2D porous molybdenum nitride/cobalt nitride heterojunction nanosheets with interfacial electron redistribution for effective electrocatalytic overall water splitting

Hao Guo, Aiping Wu*, Ying Xie, Haijing Yan, Dongxu Wang, Lei Wang and Chungui Tian*

Key Laboratory of Functional Inorganic Material Chemistry, Ministry of Education of China, Heilongjiang University, Harbin 150080, China

E-mail: wap1612@163.com; chunguitianhq@163.com; tianchungui@hlju.edu.cn.

Table of Contents

Experimental section

12. **Figure S11.** (a) XRD pattern and (b) SEM image of Mo_2N-Co_xN-5-0.5, (c) XRD pattern and (d) SEM image of Mo_2N-Co_xN-5-2, (e) XRD pattern and (f) SEM image of Mo_2N-Co_xN-5-5.
13. **Figure S12.** (a) SEM, (b, c) TEM, (d) STEM images and corresponding EDS elemental mapping of 2D Co-W-O precursor nanosheets.
14. **Figure S13.** (a) SEM, (b, c) TEM, (d) STEM images and corresponding EDS elemental mapping of 2D Co-V-O precursor nanosheets.
15. **Figure S14.** (a) XRD pattern, (b) SEM, (c) TEM, (d) STEM images and corresponding EDS elemental mapping of WN-Co_xN sample.
16. **Figure S15.** (a) XRD pattern, (b) SEM, (c) TEM, (d) STEM images and corresponding EDS elemental mapping of VN-Co_xN sample.
17. **Figure S16.** LSV curves of the NF and Mo_xN for HER.
18. **Figure S17.** Polarization curves of Co_xN, Mo_2N-Co_xN-4, Mo_2N-Co_xN-5 and Mo_2N- Co_xN-6 for HER with 90 % iR-correction.
19. **Figure S18.** (a) LSV curves and (b) Tafel slopes of Mo_2N-Co_xN-5-0.5, Mo_2N-Co_xN-5-2 and Mo_2N-Co_xN-5-5 for HER.
20. **Figure S19.** CVs of the catalysts recorded from 0.12 to 0.22 V at different rates from for 10 to 60 mV s^{-1} for (a) Co_xN, (b) Mo_2N-Co_xN-4, (c) Mo_2N-Co_xN-5, and (b) Mo_2N-Co_xN-6 in 1.0 M KOH for HER.
21. **Figure S20.** CVs of the catalysts recorded from 0.12 to 0.22V at different rates from 10 to 60 mV s^{-1} for (a) Mo_2N-Co_xN-5-0.5, and (b) Mo_2N-Co_xN-5-2 and (c) Mo_2N-Co_xN-5-5 in 1.0 M KOH, and (d) The capacitive current at 0.17 V as a function of the scan rate for Mo_2N-Co_xN-5-0.5, Mo_2N-Co_xN-5-2 and Mo_2N-Co_xN-5-5 for HER.
22. **Figure S21.** The LSV curves of Co_xN, Mo_2N-Co_xN-4, Mo_2N-Co_xN-5 and Mo_2N-Co_xN-6 for HER normalized by ECSA.
23. **Figure S22.** Nitrogen adsorption-desorption isotherms of Co_xN and Mo_2N-Co_xN-5.
24. **Figure S23.** CVs of (a) Co_xN, (b) Mo_2N-Co_xN-5-0.5, (c) Mo_2N-Co_xN-5, (d) Mo_2N-Co_xN-5-2, (e) Mo_2N-Co_xN-5-5, in 1.0 M PBS (pH=7) with a scan rate of 50 mV dec^{-1}. (f) The calculated turnover frequency curve of Co_xN, Mo_2N-Co_xN-5-0.5, Mo_2N-Co_xN-5, Mo_2N-Co_xN-5-2, Mo_2N-Co_xN-5-5 catalysts for HER.
25. **Figure S24.** Nyquist plots of (a) Mo_2N-Co_xN-4, Mo_2N-Co_xN-5 and Mo_2N-Co_xN-6 and (b) Mo_2N-

40. **Figure S39.** (a, b) Top-view and Side-view schematic models of Mo_2N-CoN (Co-2-site) with H* adsorbed on its surface.
41. **Figure S40.** (a, b) Top-view and Side-view schematic models of Mo_2N-CoN (Mo-1-site) with H* adsorbed on its surface. (c, d) Top-view and Side-view schematic models of Mo_2N-CoN (Mo-2-site) with H* adsorbed on its surface.
42. **Table S2.** The HER performance of different catalysts in 1M KOH medium.
43. **Table S3.** Comparison of HER performance of Mo_2N-Co_xN-5 with other non-noble metal HER electrocatalysts in alkaline condition.
44. **Table S4.** The OER performance of different catalysts.
45. **Table S5.** Comparison of OER performance of Mo_2N-Co_xN-5 with other non-noble metal OER electrocatalysts in alkaline conditions.
46. **Table S6.** Comparison of the overall water splitting performance of this work in alkaline electrolytes with literature reports.

Experimental section

Materials and chemicals

All chemicals were used as received without further purification. Sodium molybdate dihydrate ($Na_2MoO_4 \cdot 2H_2O$, purity, ≥ 99%) was purchased from Tianjin Kermel Chemical Reagent Co. Ltd. Anhydrous methanol (CH_3OH) and alcohol (CH_3CH_2OH) were purchased from Tianjin Guangfu Fine Chemical Research Institute. Cobalt nitrate hexahydrate ($Co(NO_3)_2 \cdot 6H_2O$, purity, 99%) and 2-methylimidazole ($C_4H_6N_2$, purity 98%) were purchased from Aladdin Ltd. Nafion solution (5 wt%) was purchased from Alfa Aesar. Ni Foam (NF) was purchased from Jinghong New Energy Technology Co.Ltd. (Zhengzhou, China).

Synthesis of ZIF-67 polyhedrons

The ZIF-67 polyhedrons were synthesized according to the previous report with some minor

variation. Typically, 12 mmol $Co(NO_3)_2 \cdot 6H_2O$ and 48 mmol 2-methylimidazole (2-MIM) were dissolved respectively into 300 mL methanol with stirring for 30 min. Then, the $Co(NO_3)_2 \cdot 6H_2O$ solution was poured into the 2-MIM solution and the mixed solution was continuous stirring for 6 hours at room temperature. The purple precipitate was collected via filtration and washing with methanol repeatedly. The samples were dried at 60°C overnight in a vacuum drying oven.

Synthesis of Co-Mo-O precursor nanosheets

First, 50 mg ZIF-67 were ultrasonically dispersed into 70 ml deionized water. Then, 1 mg Na_2MoO_4 were quickly added to the above solution. After stirring for 6 h, 10 mg of dopamine was added to the above solution. The solution was continuous stirring for 6 h at room temperature. Finally, the products were collected after washing/centrifuge, vacuum drying at 60°C overnight. The as-obtained products were termed as Co-Mo-O precursor nanosheets.

In order to investigate the different addition amounts of Mo in detail, a series of nanosheets were synthesized by changing the addition amount of Na_2MoO_4 using a synthesis method similar to that of Co-Mo-O precursor nanosheets. We named it Co-Mo-O-x nanosheet (x= 0.5, 2, 5).

Synthesis of 2D porous Mo_2N-Co_xN Nanosheets

To synthesize Mo_2N-Co_xN nanosheets, the Co-Mo-O nanosheet precursors were calcinated at 500°C for 3 h under NH_3 atmosphere with a heating rate of 5°C min^{-1}. The product was denoted as Mo_2N-Co_xN-5. To tune the micro-structures and composition of the Mo_2N-Co_xN nanosheets, the nitridation was also carried out at 400°C (Mo_2N-Co_xN-4) and 600°C (Mo_2N-Co_xN-6), while keeping other parameters unchanged. The samples and their corresponding synthesis parameters are shown in Table S1.

Characterizations

The transmission electron microscopy (TEM) and high resolution TEM (HRTEM) was performed on a JEM-F200 electron microscope (JEOL, Japan) with an acceleration voltage of 200 kV. X-ray photon-electron Spectroscopy (XPS) analysis was performed using a VG ESCALAB MK II spectrophotometer with Mg-Kα radiation (1253.6 eV). Scanning electron microscopy (SEM) test was carried out on a Hitachi S-4800 instrument at an accelerating voltage of 5 kV. A PE Spectrum One B IR spectrometer was used to record the fourier transform infrared spectra (FT-IR) of the samples in the region 400–4000 cm^{-1} with KBr pellets. X-ray diffraction (XRD) patterns were recorded using a Bruke D8 equipped with Cu-Ka radiation, and a Rigaku D/max-2600/PC X-ray diffractometer (XRD, Cu-Ka radiation). Thermogravimetric (TG) analysis was performed using a TA Q600 thermal analyzer under a stream of air with a heating rate of $10^{o}C\ min^{-1}$. The thickness of 2D Mo_2N-Co_xN nanosheets was analyzed by a Multimode Nanoscope VIII Atomic Force Microscope (AFM, Bruker) with mica as the base. Nitrogen adsorption–desorption isotherms were measured at 77 K on a Quantachrome autosorb iQ/ASiQwin. The Brunauer–Emmett–Teller method was used to calculate the specific surface area. Scanning Kelvin Probe (SKP) measurements (SKP5050 system, Scotland) were made in ambient atmosphere, and a gold electrode was used as the reference electrode. The work function (φ) was calculated by using the formula

$$\varphi_{Au} - \eta_{Au}/1000 = \varphi - \eta/1000$$

in which φ_{Au} is the work function of Au and η_{Au} = −239.75 eV.

Electrochemical measurements

All electrochemical measurements were carried out on a CH Instruments electrochemical workstation (CHI 760E, ShangHai) in a 1 M KOH electrolyte with a three electrode setup. An Hg/HgO

electrode and a graphite rod were used as the reference electrode and counter electrodes, respectively. The working electrode was prepared by mixing 4 mg of Mo_2N-Co_xN nanosheets, 1 mg carbon black and 30 μL Nafion (5 wt%) were dispersed in 40 μL of a mixture of water and ethanol (v : v = 1 : 1) and the mixture was treated for 30 min under ultrasound to form a homogeneous ink, subsequently, the catalyst ink was smeared onto Ni foam (1 cm ×1 cm). The Ni foam covered with Mo_2N-Co_xN nanosheets was dried at 60 °C for 12 h in a vacuum oven. Before coating, the NF was washed with acetone, HCl aqueous solution (2 M), deionied water and ethanol in sequence. The linear sweep voltammograms (LSV) test was carried out in 1 M KOH with the scan rate of 5 mV s^{-1}, which was performed after 20 cycles of cyclic voltammetry (CV) tests to steady the current. The double layer capacitances were chalk up CV, in which CV test were conducted with scan rates from 10 to 100 mV s^{-1}. The Tafel data were fitted according to the equation $\eta = b \log(j) + \alpha$ (j: current density, and b: Tafel slope). All potentials in this work were referenced to the RHE according to $E_{RHE} = E_{Hg/HgO} + 0.059 \times pH + E^{\theta}_{Hg/HgO}$. The LSV data of the typical catalysts with 90% IR compensation were also obtained by using the IR compensation function of CHI 760E electrochemical workstation.

The ECSA is the electrochemical active surface area, which can be calculated from the following formula:

$$\mathrm{ECSA} = \frac{\text{specific capacitance}}{40\ \mu\mathrm{F\ cm^{-2}\ per\ cm^2}}$$

where specific capacitance is C_{dl}, and 40 μF cm^{-2} is a constant to convert capacitance to ECSA. The specific capacitance can be converted into an electrochemical active surface area (ECSA) using the specific capacitance value for a flat standard with 1 cm^2 of real surface area.

The faradaic efficiency (FE) for HER was calculated by comparing the experimentally determined and theoretically calculated amounts of H_2 and O_2. In the test, constant potential electrolysis was performed

at 100 mA cm^{-2} for 60 minutes in a closed h-shaped electrolytic cell. The amount of gas generated was analyzed by gas chromatography (GC). The theoretical H_2 amount was calculated as follows:

$$n\ (H_2) = Q/nF$$

where $n(H_2)$ was the number of moles of hydrogen produced, Q was the charge passed through the electrodes, F was the faradaic constant (96485 C mol^{-1}), and n was the number of electrons transferred during water splitting (for HER, n was 2). The calculation of the theoretical amount of O_2 was the same as that for H_2 except n = 4.

Theoretical calculation

Density Functional Theory (DFT) simulations were performed by employing Cambridge Sequential Total Energy Package (CASTEP) module implemented in Material Studio. The generalized gradient approximation (GGA) with a Perdew-Burke-Ernzerhof (PBE) functional was used to describe the electronic exchange and correlation effects, and the kinetic energy cutoff was set to be 340 eV. The self-consistent field (SCF) tolerance was 1×10^{-6} eV and Monkhorst-Pack mesh of 3×3×1 was used to perform geometry optimization. The Gibbs free-energy of H* (ΔG_{H^*}) can be calculated by the equation $\Delta G_{H^*} = \Delta E_{H^*} + \Delta E_{ZPE} - T_{\Delta S}$, where ΔE_{H^*}, ΔE_{ZPE} and ΔS are the adsorption energy of atomic hydrogens on the given unit cell, the difference corresponding to the zero point energy between the adsorbed hydrogen and hydrogen in the gas phase and the entropy change of H* adsorption, respectively. ΔS can be obtained by $\Delta S = S_{(H^*)} - 1/2S^0_{H2}$ (S^0_{H2} is the entropy of H_2 in the gas phase at standard conditions). As the entropy of hydrogen in absorbed state is negligible, ΔS can be calculated as $-1/2S^0_{H2}$. Therefore the Gibbs free-energy of H* can be taken as: $\Delta G_{H^*} = \Delta E_{H^*} + 0.24$ eV.

Table S1. The samples synthesized under different conditions and their corresponding synthesis parameters.

Entry	Starting materials	Heating temperature (°C)	m (Mo(W/V) source) (mg)	Final samples
1	$Co(OH)_2$	500	0 mg	CoN-$Co_{5.47}N$ (Co_xN)
2	Co-Mo-O precursors	400	1 mg	Mo_2N-Co_xN-4
3	Co-Mo-O precursors	500	1 mg	Mo_2N-Co_xN-5
4	Co-Mo-O precursors	600	1 mg	Mo_2N-Co_xN-6
5	Co-Mo-O-0.5	500	0.5 mg	Mo_2N-Co_xN-5-0.5
6	Co-Mo-O-2	500	2 mg	Mo_2N-Co_xN-5-2
7	Co-Mo-O-5	500	5 mg	Mo_2N-Co_xN-5-5
8	Co-V-O precursors	500	1 mg	VN-Co_xN
9	Co-W-O precursors	500	1 mg	WN-Co_xN

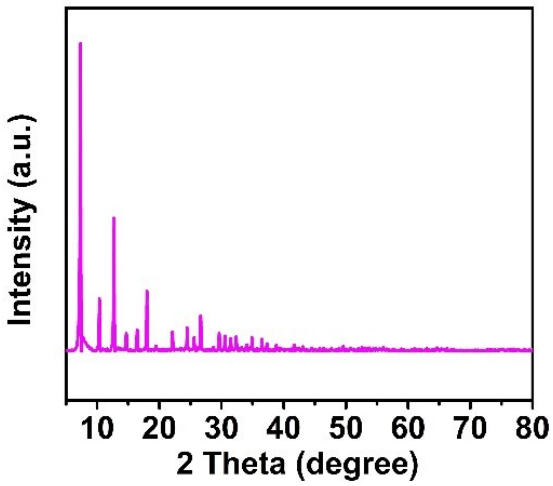

Figure S1. XRD pattern of ZIF-67.

The XRD pattern shows the characteristic peaks corresponding to ZIF-67. The peaks is completely different with that of Co-Mo-O sheets, implying the successful conversion of ZIF-67 into Co-Mo-O sheets precursor.

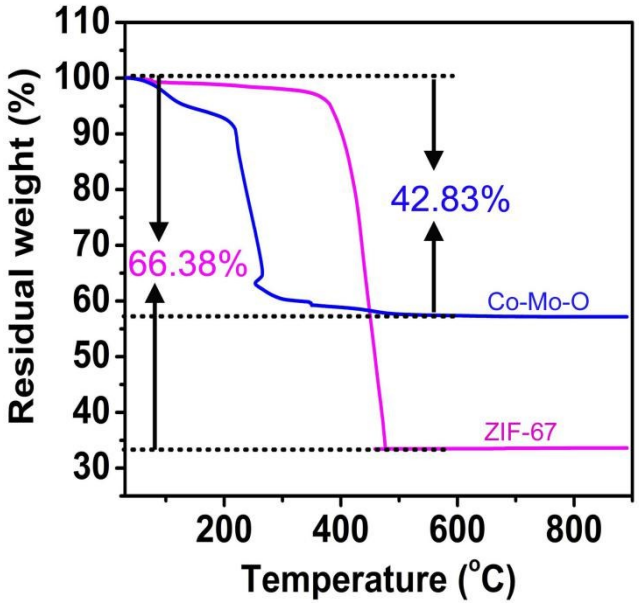

Figure S2. Thermogravimetric curves of ZIF-67 and Co-Mo-O precursor.

As shown in Figure S2, the weight abruptly loses of ZIF-67 around 400°C is caused by the collapse of the skeleton, and the final weight loss rate is less than 66.38%. For the Co-Mo-O precursor, the mass loss at 100°C is attributed to the consumption of water in the material. The subsequent quality loss is attributed to the decomposition of polydopamine. It can be seen that the quality loss of Co-Mo-O precursor is only 42.83%, which indicates that molybdate species were successfully introduced into the precursor.

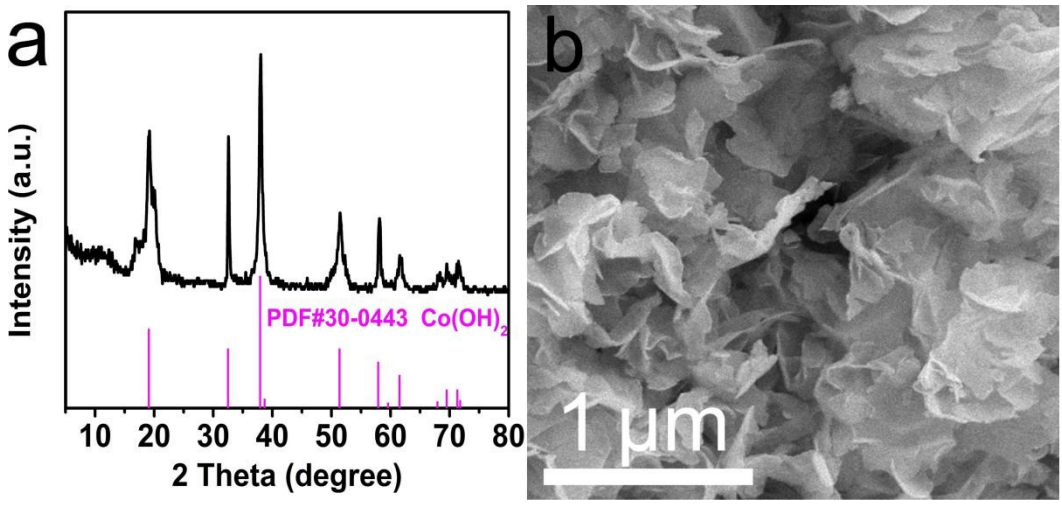

Figure S3. XRD pattern and SEM images of $Co(OH)_2$.

The sample obtained by directly etched ZIF-67 in H_2O without adding sodium molybdate were characterized by XRD and SEM. The XRD pattern of the sample shows the characteristic peak of $Co(OH)_2$ (Figure S3a), implying that the OH^- form H_2O plays main role for etching ZIF-67 in present synthesis. However, as displayed in Figure S3b, the obtained sheets have irregular morphology in this case, which shows the positive role of the Na_2MoO_4 and dopamine on the formation of regular sheets morphology.

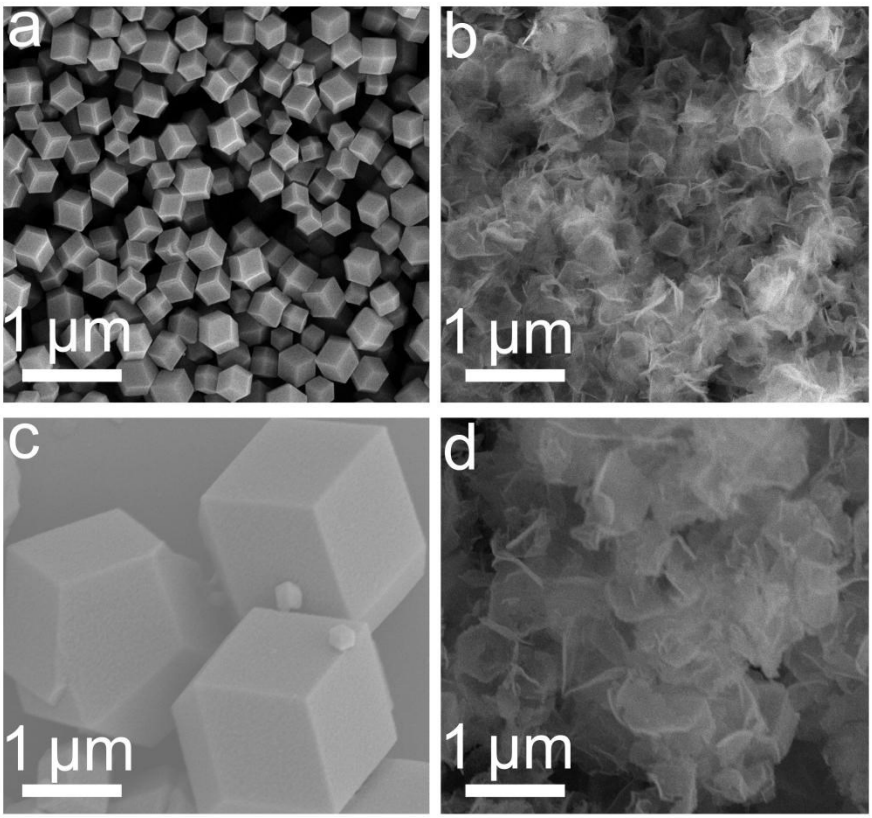

Figure S4. (a) Small-size ZIF-67, (b) small-size Co-Mo-O precursor, (c) large-size ZIF-67, (d) large-size Co-Mo-O precursor.

The size of the sheets has an important influence on the catalytic performance. In our work, the 2D Mo-Co-O nanosheets with controllable size can be obtained by adjusting the size of ZIF-67. First, the ZIF-67 with different sizes were synthesized by changing the ratio of cobalt nitrate and 2-MIM. When the ratio is 1:8, the size of the acquired ZIF-67 is about 400 nm. However, when the ratio is 1:2, the size of ZIF-67 is about 2 μm. As shown in Figure S4, using these two kinds of ZIF-67 polyhedrons as raw materials, the corresponding 2D Mo-Co-O nanosheets with different sizes can be obtained under the same experimental conditions. Therefore, compared with the traditional two-dimensional nanosheet synthesis method, the size of the nanosheets synthesized by this etching method is adjustable.

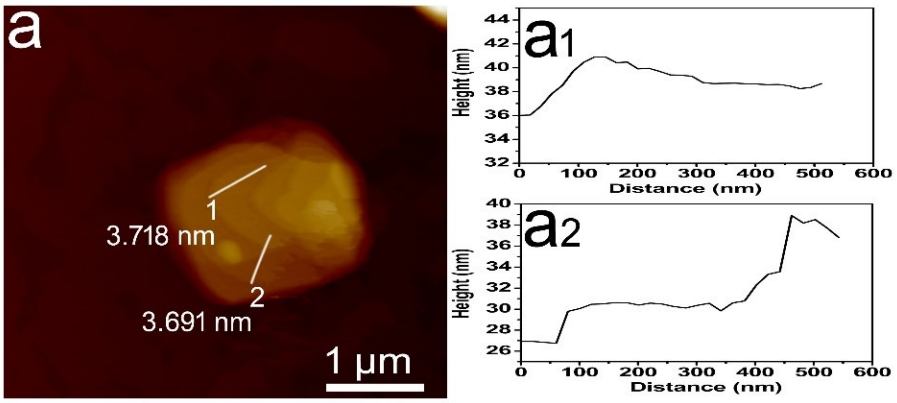

Figure S5. (a) AFM image and (a_1-a_2) corresponding height profiles along the white line of the Mo_2N-Co_xN-5.

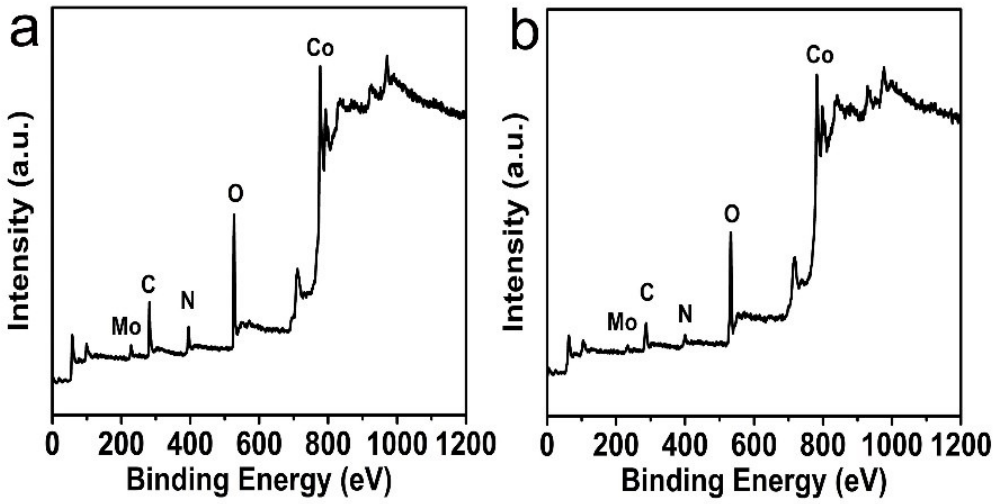

Figure S6. XPS survey spectrum of (a) Co-Mo-O precursor and (b) Mo_2N-Co_xN-5.

The XPS survey spectra of the Co-Mo-O precursor and Mo_2N-Co_xN-5 reveal the presence of Co, O, Mo and N elements.

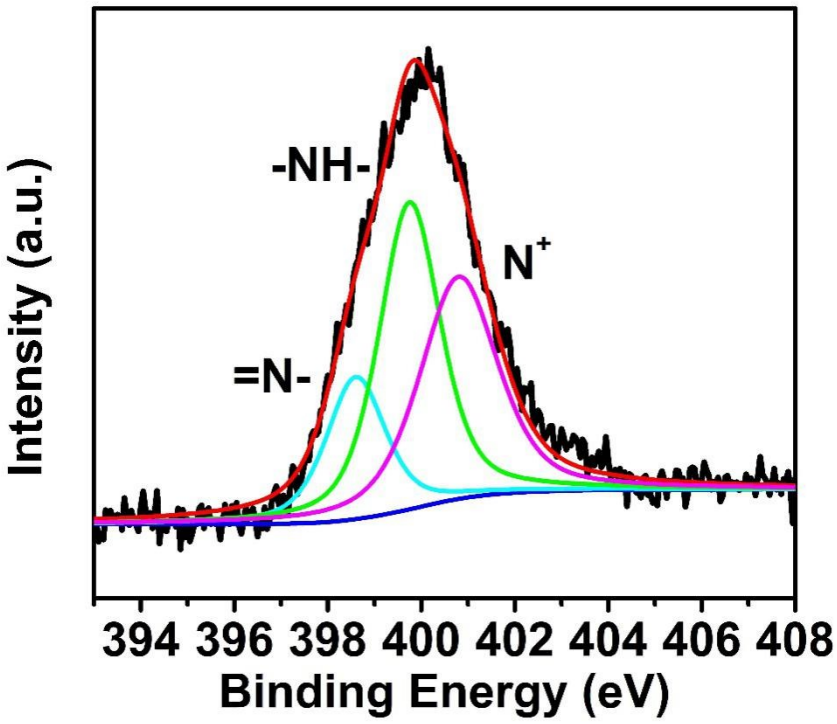

Figure S7. N 1s spectrum of Co-Mo-O precursor.

The high resolution N 1s XPS spectrum shows three peaks belonging to =N-(398.6 eV), -NH- (399.6 eV) and N^+ (400.8 eV) in dopamine.

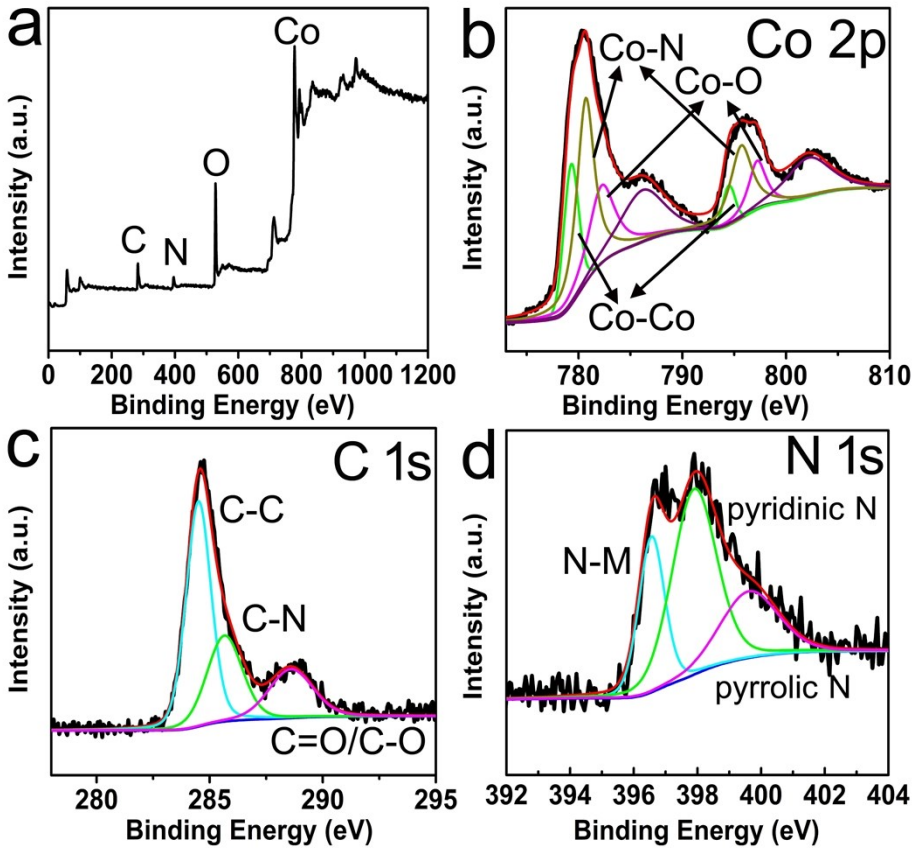

Figure S8. XPS spectra of Co_xN :(a) wide scan spectrum and the high-resolution spectra of (b) Co 2p, (c) C 1s and (d) N 1s.

Figure S8a shows the broad spectrum of Co_xN, and the results show the presence of Co, C, N, and O elements in Co_xN. Figure S8b displays the Co 2p high-resolution spectra. The peaks at 781.8 and 796.8 eV correspond to Co $2p_{3/2}$ and Co $2p_{1/2}$ of Co^{2+} in CoO_x. The peaks of 780.2 and 795.2 eV are attributed to Co $2p_{3/2}$ and Co $2p_{1/2}$ of Co^{3+} in Co_xN. The peaks at 778.82 and 793.8 eV are ascribed to the Co $2p_{3/2}$ and Co $2p_{1/2}$ can be assigned to Co-Co in Co_xN. The high-resolution spectrum of C 1s shows three peaks, namely C-C (284.5 eV), C-N (285.6 eV), and C-O/C=O (288.6 eV). The high-resolution N 1s XPS peak shows that the three peaks at 399.6, 397.9 and 396.5 eV can be attributed to pyrrole N, pyridine N and N-M, respectively.

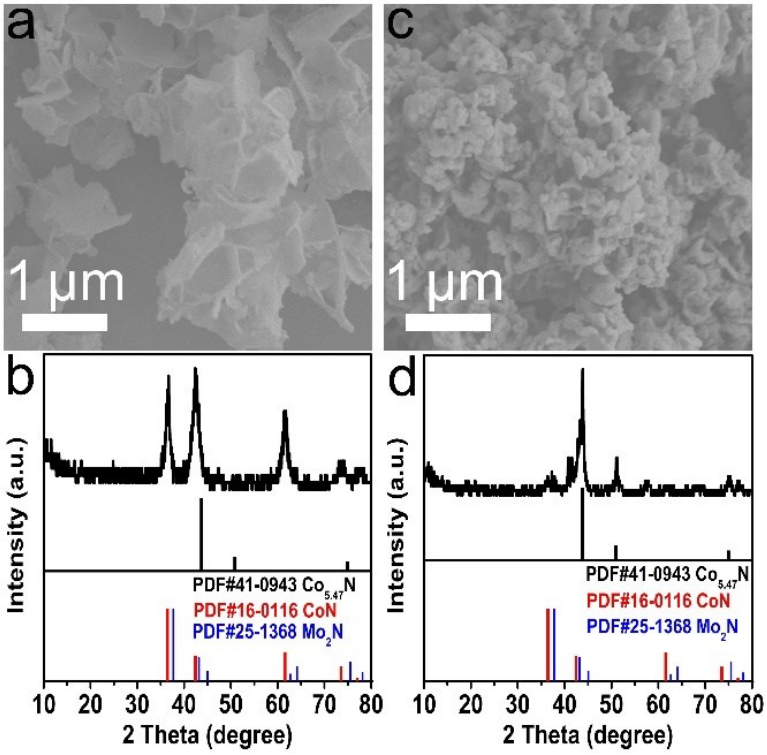

Figure S9. (a) SEM image and (b) XRD pattern of Mo_2N-Co_xN-4, (c) SEM image and (d) XRD pattern of Mo_2N-Co_xN-6.

Figure S9a shows the SEM image of Mo_2N-Co_xN-4. The morphology of the nanosheets are preserved, which is similar to the precursor. When the temperature rises to 600°C, the sample shows the obvious aggregation, which is not conducive to improving the catalytic performance. This morphology will reduce the exposure of active sites, which is not conducive to electrocatalytic reactions. Figure S9b and S9d show the patterns of the Mo_2N-Co_xN-4 and Mo_2N-Co_xN-6 catalysts. It can be seen that the peak positions is the same as that of Mo_2N-Co_xN-5 sample, but the intensity has a certain change, indicating the crystallinity of the catalysts can be effectively controlled.

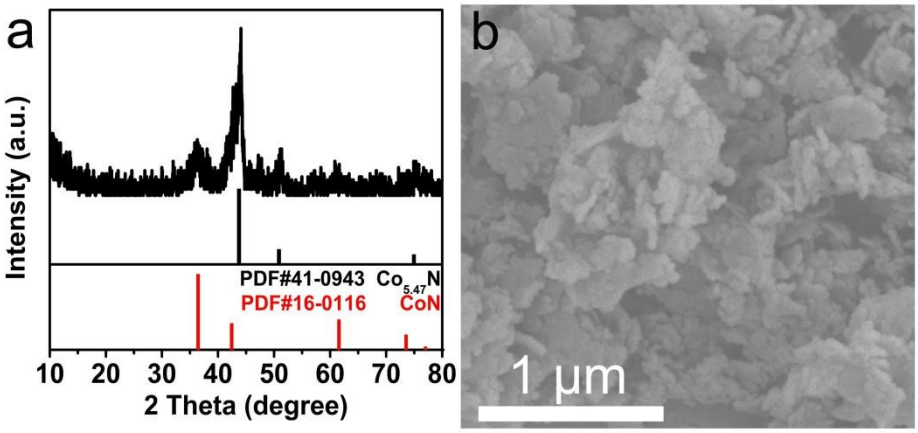

Figure S10. XRD pattern and SEM image of CoN-$Co_{5.47}N$ (Co_xN).

Figure S10a shows the XRD pattern of Co_xN. The diffraction peaks at 43.7, 50.8 and 74.9° are corresponded well to the (111), (200) and (220) planes of the $Co_{5.47}N$ phase (PDF# 41-0943). The other diffraction peaks located at 36.2, 42.2, 61.3 and 73.3°can be well-indexed to the (111), (200), (220) and (311) planes of the CoN phase (PDF# 16-0116). As shown in the SEM image (Figure S10b), there are obvious aggregation for CoN-$Co_{5.47}N$ samples, indicating the role of Mo species for the stabilization of the samples during the calcination.

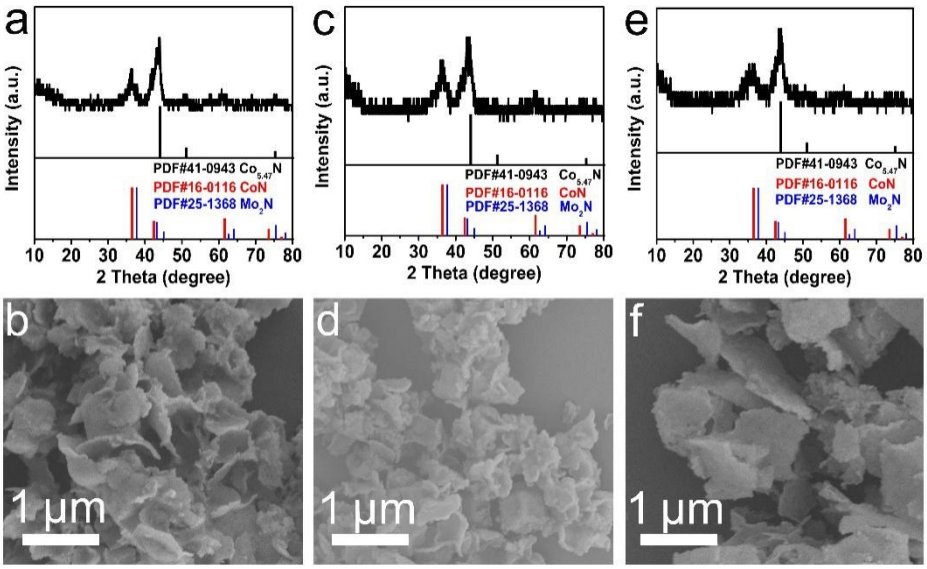

Figure S11. (a) XRD pattern and (b) SEM image of Mo_2N-Co_xN-5-0.5, (c) XRD pattern and (d) SEM image of Mo_2N-Co_xN-5-2, (e) XRD pattern and (f) SEM image of Mo_2N-Co_xN-5-5.

To obtain the optimal catalyst, a series of nanosheets catalysts with different Mo content were synthesized by changing the addition amount of Na_2MoO_4. As shown in Figure S11a-11c, the XRD patterns of Mo_2N-Co_xN-5-0.5, Mo_2N-Co_xN-5-2 and Mo_2N-Co_xN-5-5 are similar with that of Mo_2N-Co_xN-5 sample, indicating that the crystal phase has not changed. In addition, the morphology of the Mo_2N-Co_xN-5-0.5, Mo_2N-Co_xN-5-2 and Mo_2N-Co_xN-5-5 samples maintain the sheet-like structure very well, further proving the role of Mo species in the stabilization of the samples during the calcination.

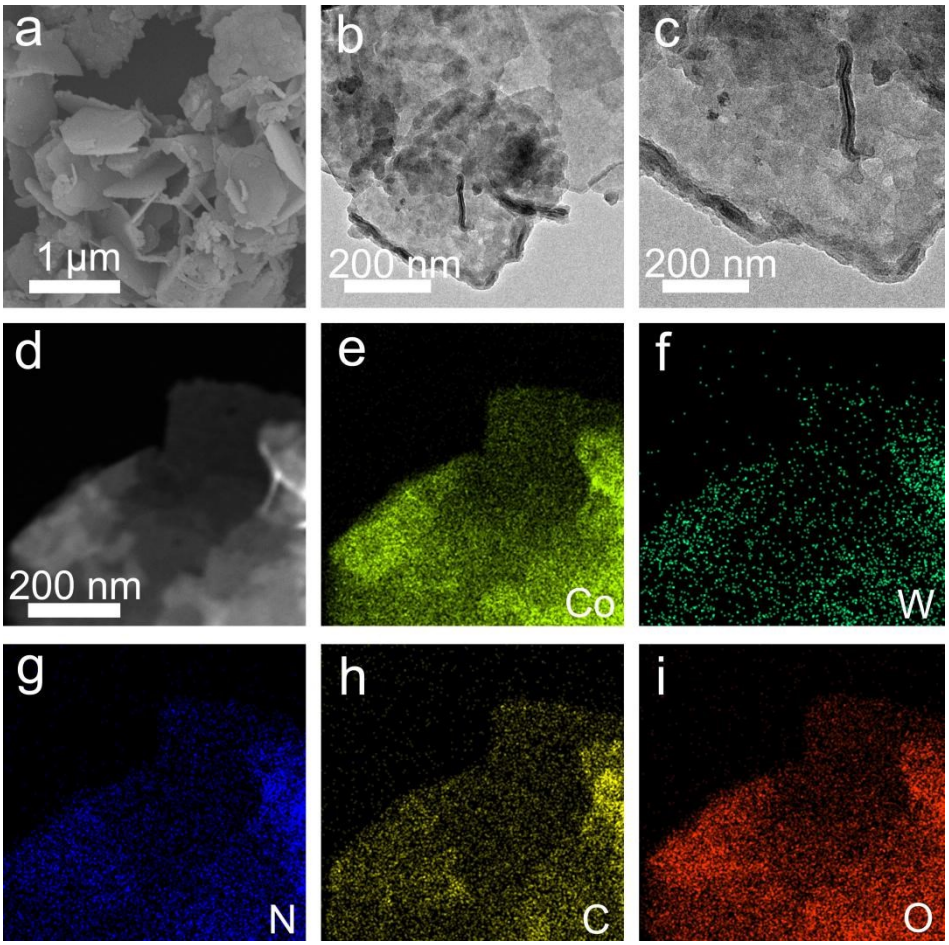

Figure S12. (a) SEM, (b, c) TEM, (d) STEM images and corresponding EDS elemental mapping of 2D Co-W-O precursor nanosheets.

Typically, by replacing molybdates with the tungstates, the corresponding W species modified $Co(OH)_2$ sheets can be obtained. The SEM and TEM images show that the obtained Co-W-O precursor exhibits a well sheet-like structure and the EDS mapping confirm the uniform distribution of each element throughout the 2D nanosheets.

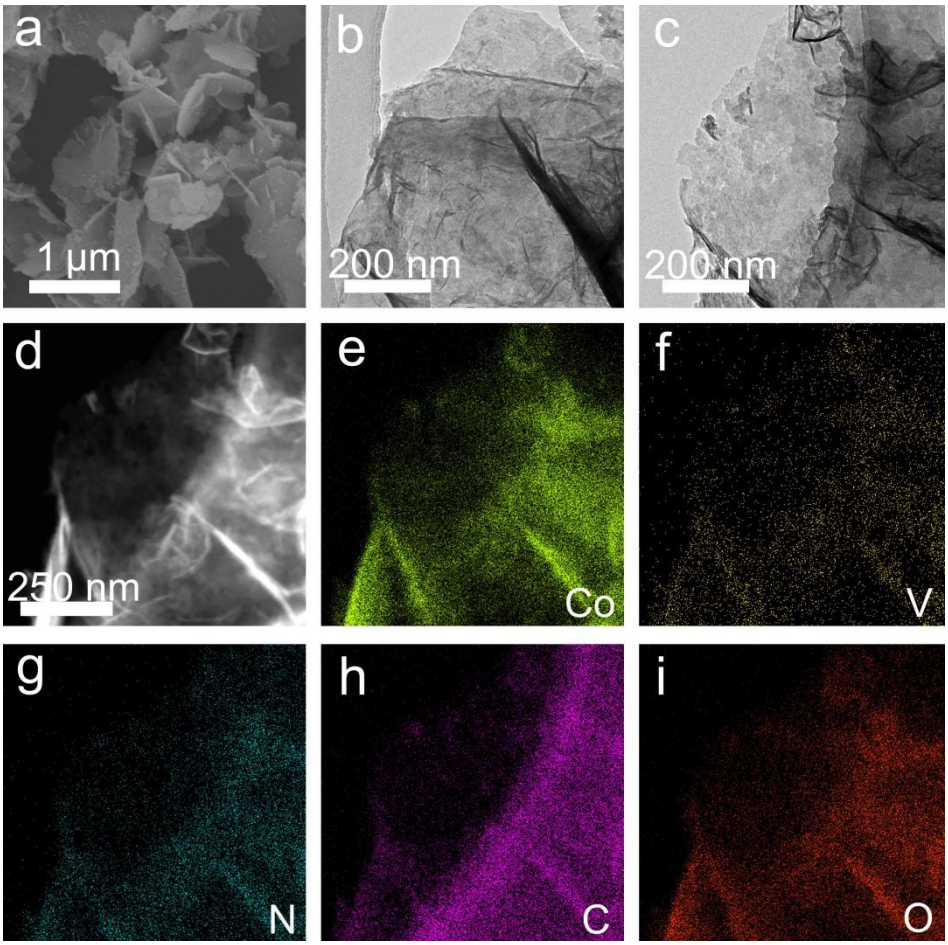

Figure S13. (a) SEM, (b, c) TEM, (d) STEM images and corresponding EDS elemental mapping of 2D Co-V-O precursor nanosheets.

Typically, by replacing molybdates with the vanadates, the corresponding V species modified $Co(OH)_2$ sheets can be obtained. The SEM and TEM images show that the obtained Co-V-O precursor exhibits a well sheet-like structure and the EDS mapping confirm the uniform distribution of each element throughout the 2D nanosheets.

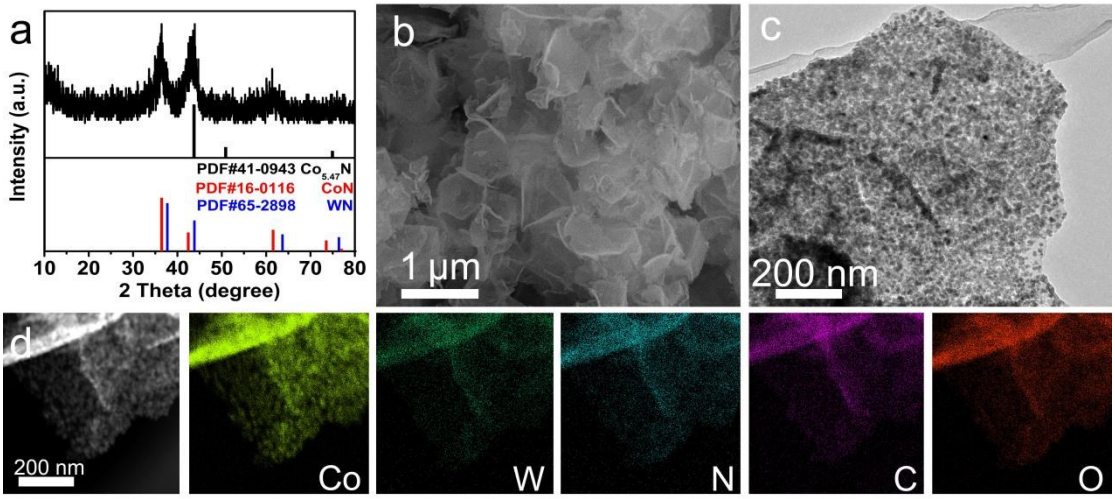

Figure S14. (a) XRD pattern, (b) SEM, (c) TEM, (d) STEM images and corresponding EDS elemental mapping of WN-Co_xN sample.

As shown in Figures S14, the corresponding WN-Co_xN catalysts can be obtained after the nitridation of Co-W-O precursors. The morphology of the WN-Co_xN catalyst remains 2D sheets structure without aggregation and the TEM image prove that there are lots of pores on the nanosheets. The STEM image and EDS elemental mapping further display the sheet structure with uniform element distribution.

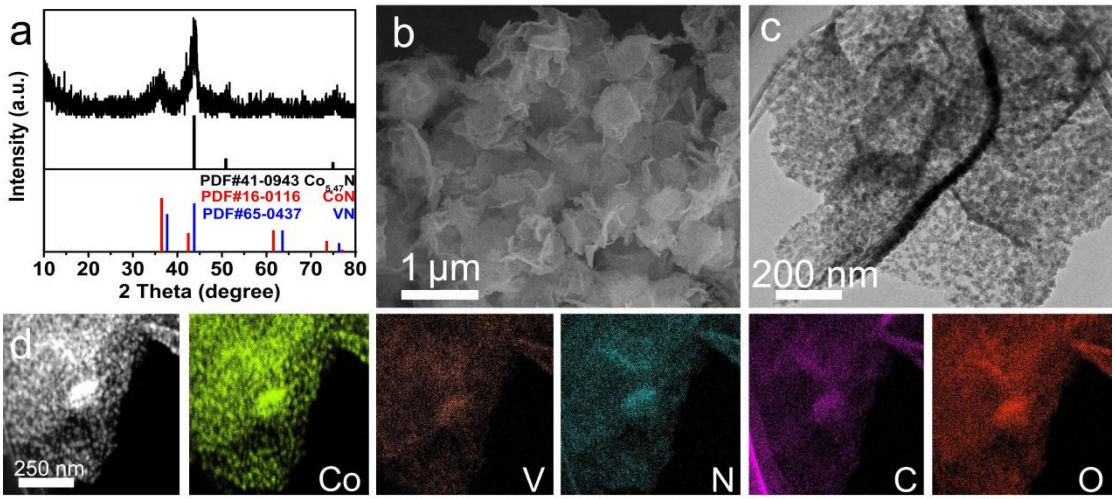

Figure S15. (a) XRD pattern, (b) SEM, (c) TEM, (d) STEM images and corresponding EDS elemental mapping of VN-Co_xN sample.

As shown in Figures S15, the corresponding VN-Co_xN catalysts can be obtained after the nitridation of Co-V-O precursors. The morphology of the VN-Co_xN catalyst still remains a sheet-like structure without aggregation. The TEM image furthe prove the porous sheet structure of VN-Co_xN. In addition, the STEM image and EDS elemental mapping also display the sheet structure with uniform element distribution.

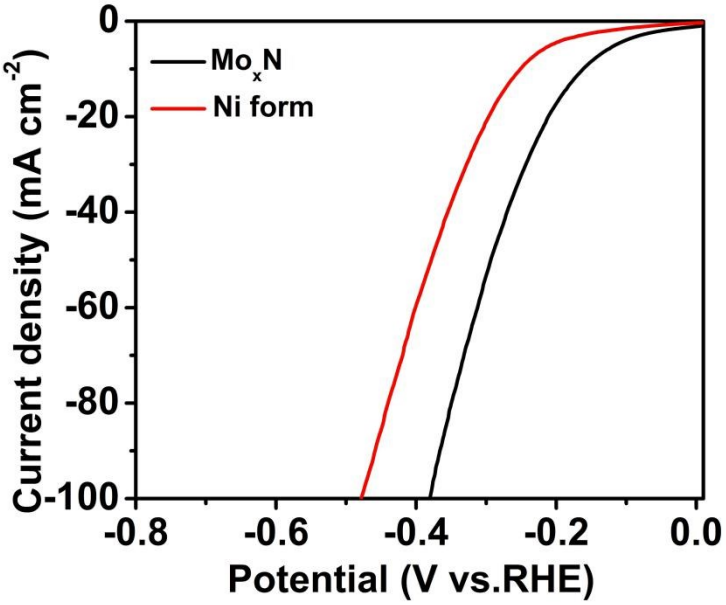

Figure S16. LSV curves of the NF and Mo_xN for HER.

The LSV curves for NF and Mo_xN show that the pristine nickel foam and Mo_xN exhibit very poor HER performance with a high overpotential of 252 mV and 161 mV at 10 mA cm^{-2}.

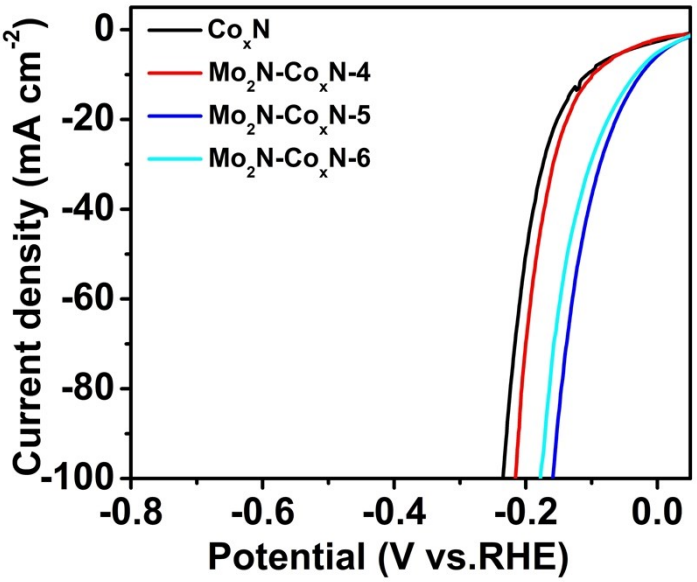

Figure S17. Polarization curves of Co_xN, Mo_2N-Co_xN-4, Mo_2N-Co_xN-5 and Mo_2N- Co_xN-6 for HER with 90 % iR-correction.

After 90% IR compensation, the Mo_2N-Co_xN-5 only needs an overpotential of 26 and 159 mV to achieve a current density of 10 and 100 mA cm^{-2}, which is much lower than those of Co_xN (107 and 234 mV), Mo_2N-Co_xN-4 (98 and 215 mV), Mo_2N-Co_xN-6 (34 and 177 mV).

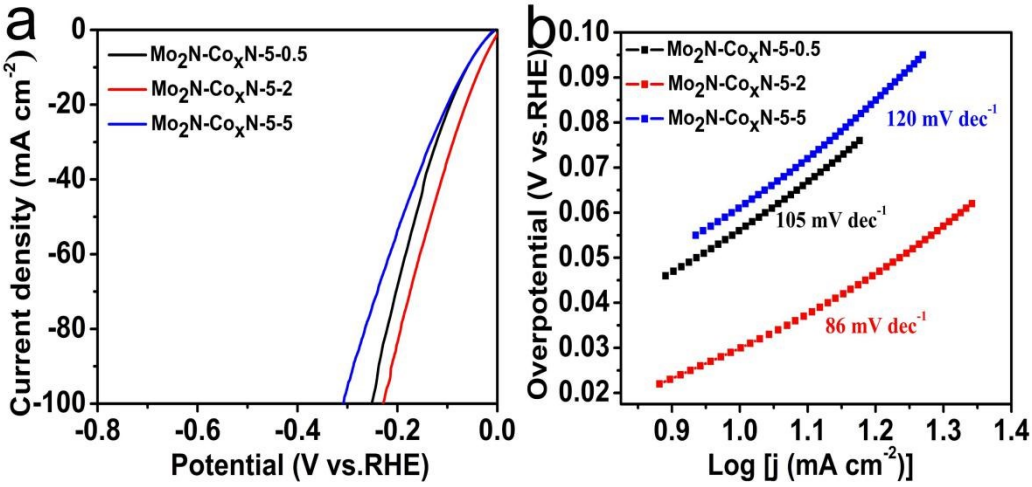

Figure S18. (a) LSV curves and (b) Tafel slopes of Mo_2N-Co_xN-5-0.5, Mo_2N-Co_xN-5-2 and Mo_2N-Co_xN-5-5 for HER.

The LSV curves of Mo_2N-Co_xN-5-0.5, Mo_2N-Co_xN-5-2 and Mo_2N-Co_xN-5-5 are shown in Figure S18a. The Mo_2N-Co_xN-5 catalyst requires overpotentials of 29 mV at 10 mA cm^{-2}. However, the values for Mo_2N-Co_xN-5-0.5, Mo_2N-Co_xN-5-2 and Mo_2N-Co_xN-5-5 samples are approximately 61, 33 and 61 mV, respectively. In addition, the Tafel slope of Mo_2N-Co_xN-5-0.5, Mo_2N-Co_xN-5-2 and Mo_2N-Co_xN-5-5 are about 105, 86 and 120 mV dec^{-1}, respectively. The above results indicate that the 2D porous Mo_2N-Co_xN-5 heterojuncion shows the lowest overpotential and smallest Tafel slope among various control samples, further suggesting the importance of constructing suitable interface for high-effective HER.

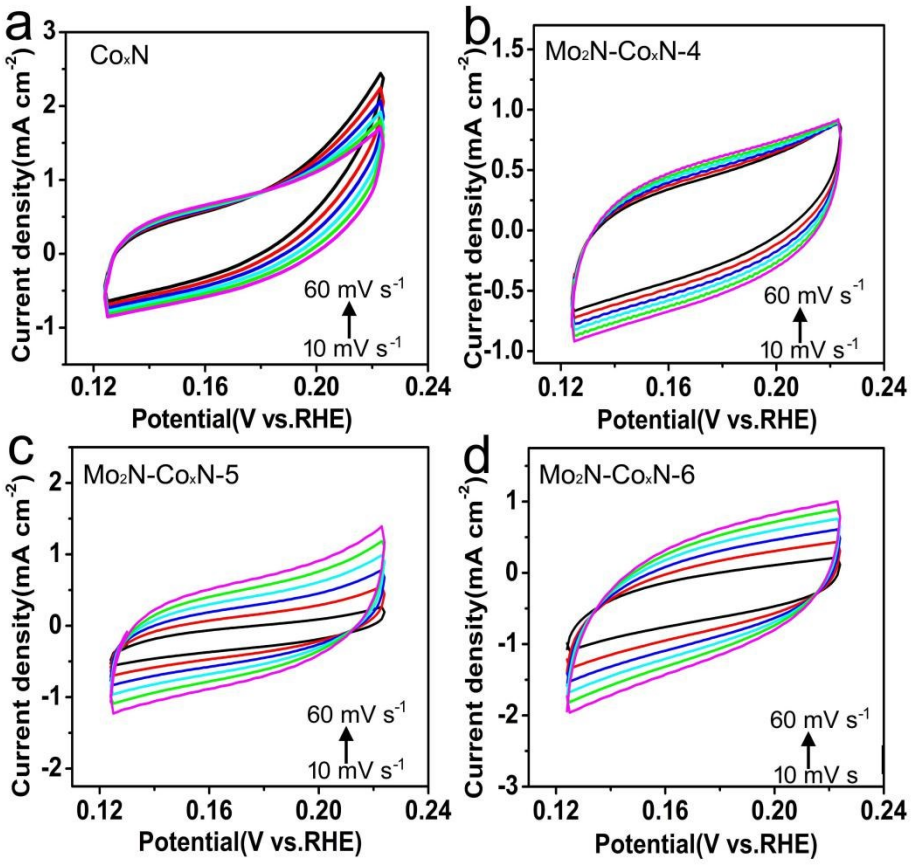

Figure S19. CVs of the catalysts recorded from 0.12 to 0.22 V at different rates from for 10 to 60 mV s^{-1} for (a) Co_xN, (b) Mo_2N-Co_xN-4, (c) Mo_2N-Co_xN-5, and (b) Mo_2N-Co_xN-6 in 1.0 M KOH for HER.

The C_{dl} value can be extracted from CV curves against different scan rates. Specially, the current responses in the voltage window of 0.12~0.22 V vs. RHE are recorded with an increased scan rate from 10 mV s^{-1} to 60 mV s^{-1} in our work. The value of Mo_2N-Co_xN-5 is close to 10.34 mF cm^{-2}, which is larger than those of Co_xN (4.01 mF cm^{-2}), Mo_2N-Co_xN-4 (4.21 mF cm^{-2}), and Mo_2N-Co_xN-6 (9.23 mF cm^{-2}). The largest C_{dl} value of Mo_2N-Co_xN-5 indicates the more catalytic active sites of Mo_2N-Co_xN-5 than other samples, contributing to its good HER performance.

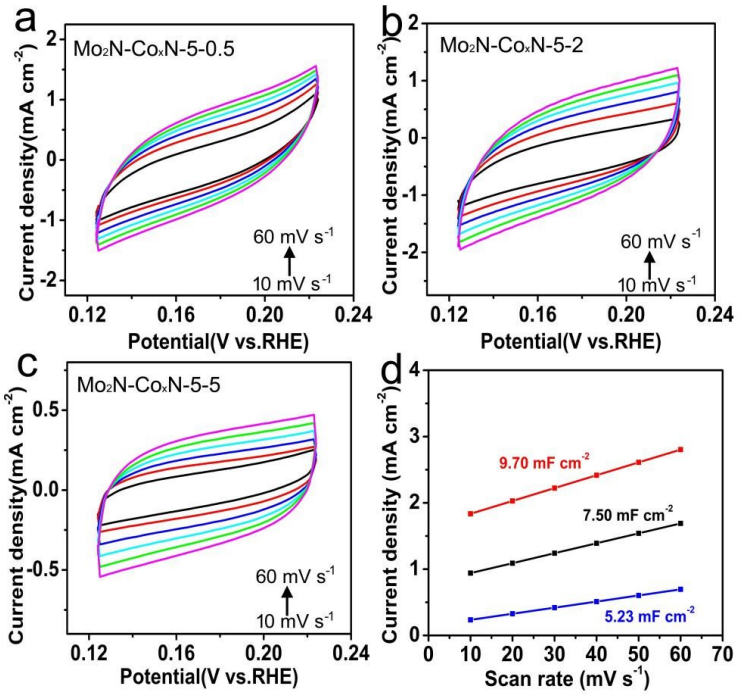

Figure S20. CVs of the catalysts recorded from 0.12 to 0.22V at different rates from 10 to 60 mV s^{-1} for (a) Mo_2N-Co_xN-5-0.5, and (b) Mo_2N-Co_xN-5-2 and (c) Mo_2N-Co_xN-5-5 in 1.0 M KOH. and (d) The capacitive current at 0.17 V as a function of the scan rate for Mo_2N-Co_xN-5-0.5, Mo_2N-Co_xN-5-2 and Mo_2N-Co_xN-5-5 for HER.

The C_{dl} value can be extracted from CV curves against different scan rates. Specially, the current responses in the voltage window of 0.12~0.22 V vs. RHE are recorded with an increased scan rate from 10 mV s^{-1} to 60 mV s^{-1} in our work. The C_{dl} value of Mo_2N-Co_xN-5-0.5, Mo_2N-Co_xN-5-2 and Mo_2N-Co_xN-5-5 were 7.50, 9.70 and 5.23 mF cm^{-2}, respectively.

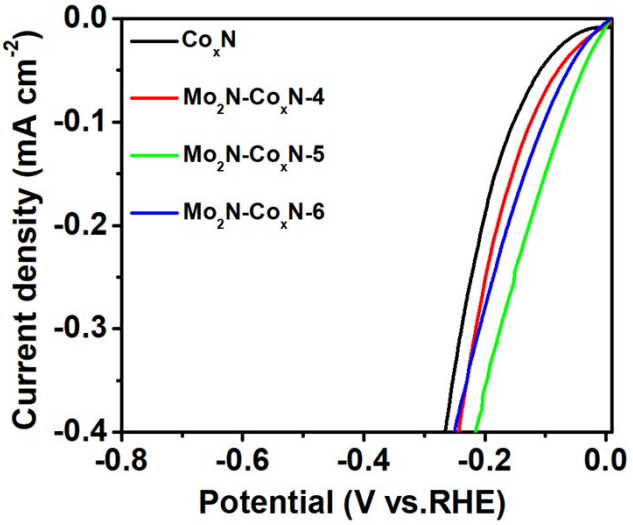

Figure S21. The LSV curves of Co_xN, Mo_2N-Co_xN-4, Mo_2N-Co_xN-5 and Mo_2N-Co_xN-6 for HER normalized by ECSA.

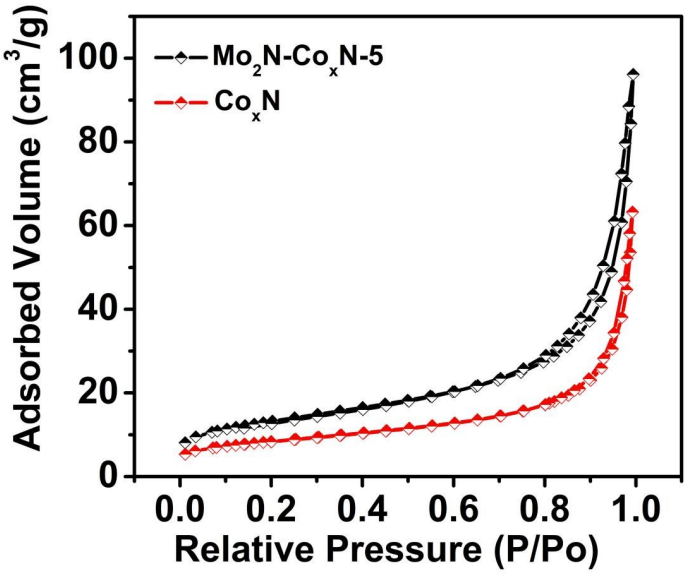

Figure S22. Nitrogen adsorption-desorption isotherms of Co_xN and Mo_2N-Co_xN-5.

The specific surface area (S_{BET}) of the Mo_2N-Co_xN-5 is about 47.42 m^2 g^{-1}. However, the S_{BET} of Co_xN is about 29.86 m^2 g^{-1}. The large S_{BET} of Mo_2N-Co_xN-5 heterojunction can provide fast mass transfer and also facilitate the exposure of active sites, which is also beneficial to improve the performance.

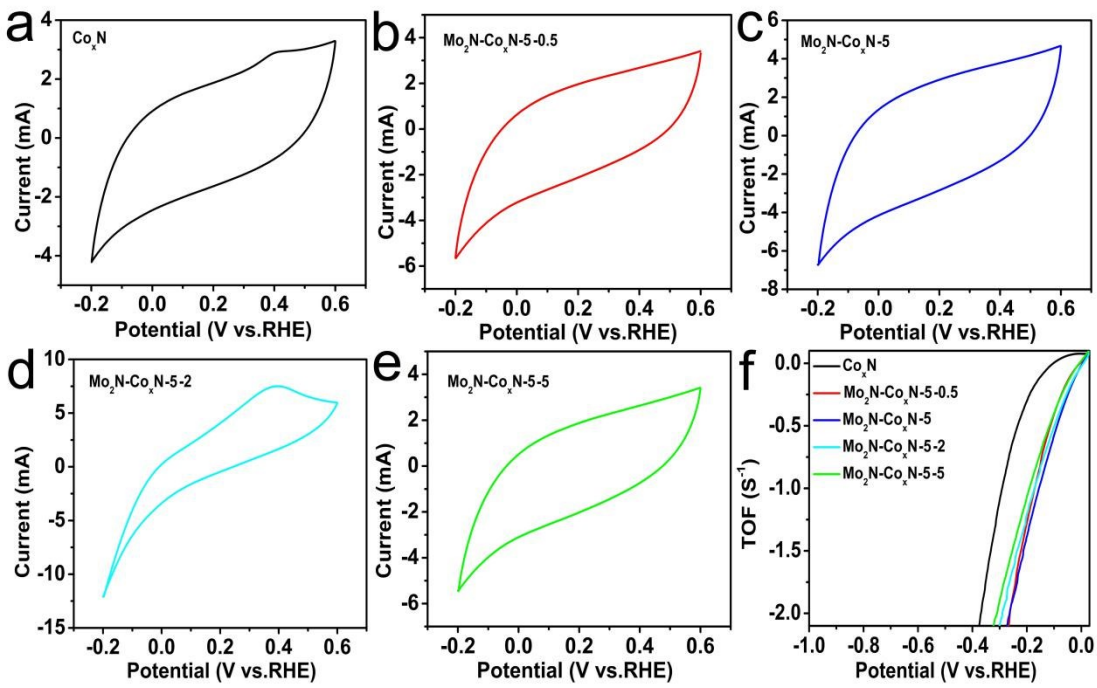

Figure S23. CVs of (a) Co_xN, (b) Mo_2N-Co_xN-5-0.5, (c) Mo_2N-Co_xN-5, (d) Mo_2N-Co_xN-5-2, (e) Mo_2N-Co_xN-5-5, in 1.0 M PBS (pH=7) with a scan rate of 50 mV dec^{-1}. (f) The calculated turnover frequency curve of Co_xN, Mo_2N-Co_xN-5-0.5, Mo_2N-Co_xN-5, Mo_2N-Co_xN-5-2, Mo_2N-Co_xN-5-5 catalysts for HER.

The TOF was calculated based on a previously reported method. Typically, the intrinsic catalytic activity is measured by the TOF of each active site. We attempt to quantify the active sites by electrochemistry. Figure S23a-e show the cyclic voltammograms of the catalyst in the range of -0.2 V to 0.6 V vs. RHE at pH 7. The integrated charge over the whole potential range should be proportional to the total number of active sites. Figure S23f shows TOF of different samples. The TOF of Mo_2N-Co_xN-5 is 0.575 s^{-1} at an overpotential of 100 mV, which is higher than Co_xN (0.005 s^{-1}), Mo_2N-Co_xN-5-0.5(0.407 s^{-1}), Mo_2N-Co_xN-5-2(0.507 s^{-1}), Mo_2N-Co_xN-5-5 (0.397 s^{-1}) in 1.0 M KOH, respectively. The high TOF value means that Mo_2N-Co_xN-5 catalyst has high intrinsic activity, which is responsible to its good HER performance.

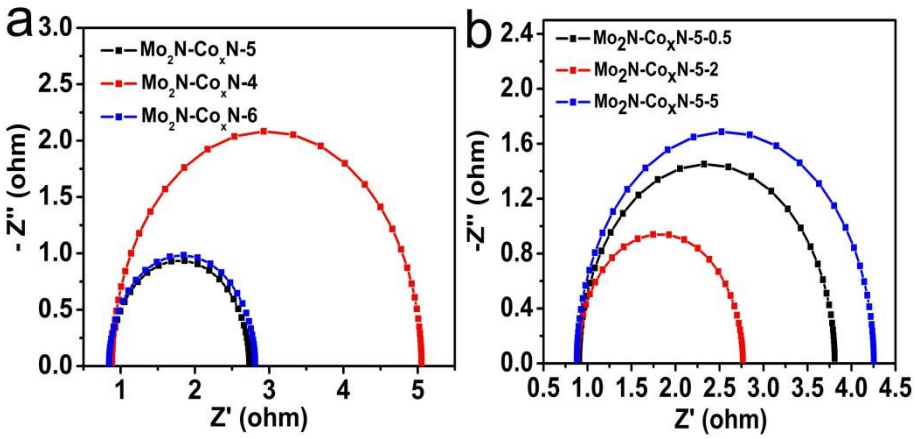

Figure S24. Nyquist plots of (a) Mo_2N-Co_xN-4, Mo_2N-Co_xN-5 and Mo_2N-Co_xN-6 and (b) Mo_2N-Co_xN-5-0.5, Mo_2N-Co_xN-5-2, Mo_2N-Co_xN-5-5 for HER.

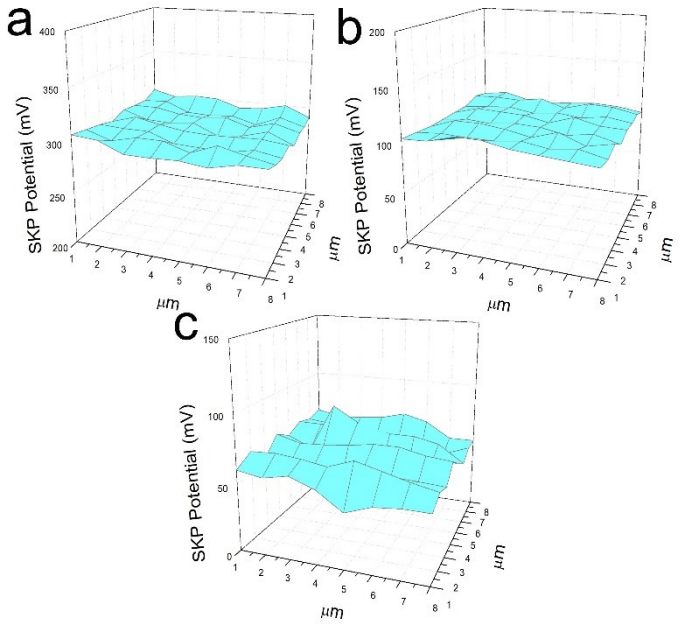

Figure S25. Work function (WF) drawings of (a) Pt/C, (b) Mo_2N-Co_xN-5 and (c) Co_xN.

The WF values of Pt/C, Mo_2N-Co_xN-5 and Co_xN are about 5.63 eV, 5.44 eV and 5.39 eV (Figure S25) by SKP test, respectively. Compared with Co_xN, the WF of Mo_2N-Co_xN-5 is close to Pt/C (5.63 eV), which indicates that the ability to capture electrons is enhanced after the formation of the Mo_2N-Co_xN-5 heterojunction. The strong ability makes the easy reduction of H* to H_2 on 2D Mo_2N-Co_xN-5 heterojunction nanosheets, thus giving enhanced HER activity.

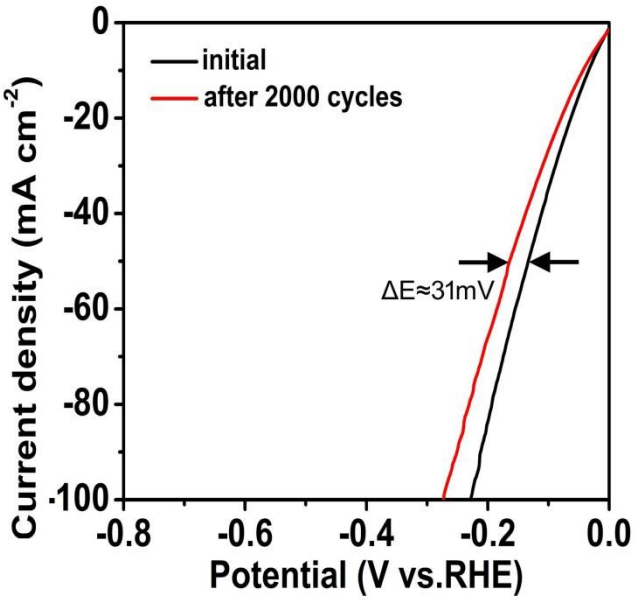

Figure S26. LSV curves of catalyst prepared without adding dopamine before and after 2000 CV cycles.

As shown in Figure S26, the HER performance of the catalyst prepared without adding dopamine is significantly decreased after 2000 CV cycles. The overpotential difference is about 31mV at a current density of 50 mA cm^{-2} after 2000 CV cycles, indicating the positive role of the carbon layer on promoting the catalytic stability.

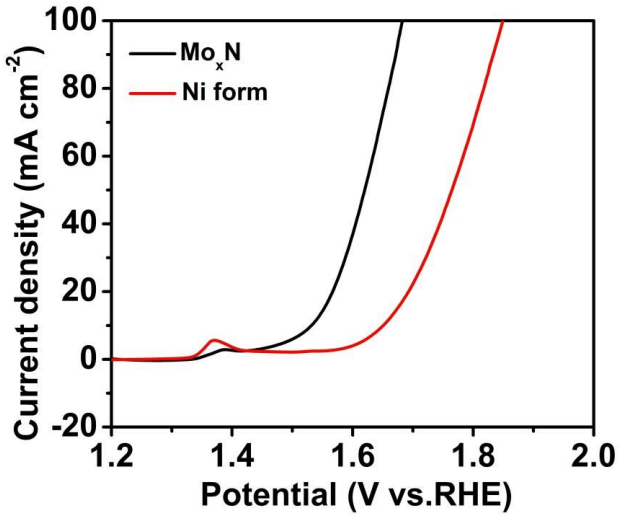

Figure S27. LSV curves of the NF and Mo_xN for OER.

The LSV curves for NF and Mo_xN show that the pristine nickel foam and Mo_xN exhibit very poor OER performance with a high overpotential of 420 and 300 mV at 10 mA cm^{-2}.

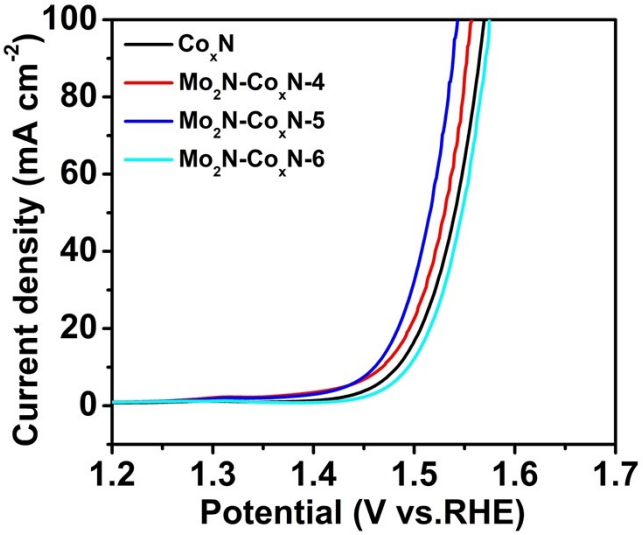

Figure S28. Polarization curves of Co_xN, Mo_2N-Co_xN-4, Mo_2N-Co_xN-5 and Mo_2N- Co_xN-6 for OER with 90 % iR-correction.

After 90% IR compensation, the Mo_2N-Co_xN-5 only needs an overpotential of 231 and 323 mV to achieve a current density of 10 and 100 mA cm^{-2}, which is much lower than those of Co_xN (253 and 339 mV), Mo_2N-Co_xN-4 (238 and 330 mV), Mo_2N-Co_xN-6 (262 and 341 mV).

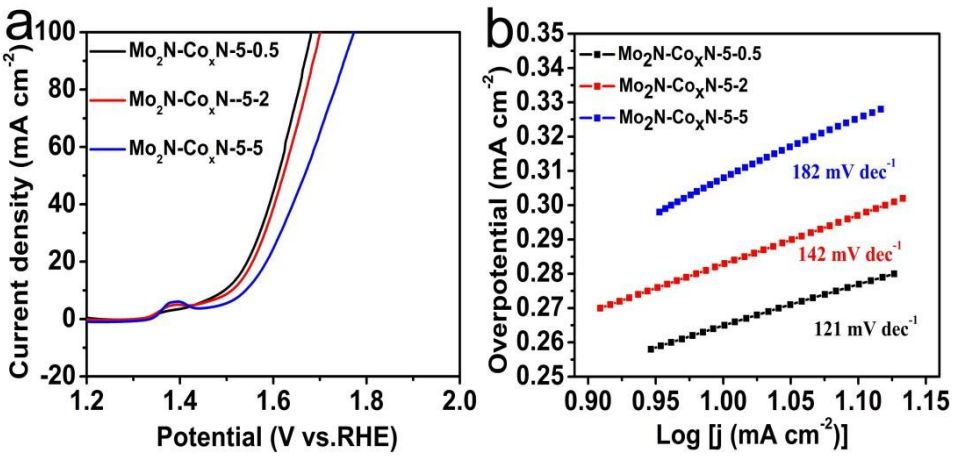

Figure S29. (a) LSV curves and (b) Tafel slopes of Mo_2N-Co_xN-5-0.5, Mo_2N-Co_xN-5-2 and Mo_2N-Co_xN-5-5 for OER.

The LSV curves of Mo_2N-Co_xN-5-0.5, Mo_2N-Co_xN-5-2 and Mo_2N-Co_xN-5-5 are shown in Figure S26a. The Mo_2N-Co_xN-5 catalyst requires overpotentials of 247 mV to reach 10 mA cm^{-2}. However, the values for Mo_2N-Co_xN-5-0.5, Mo_2N-Co_xN-5-2 and Mo_2N-Co_xN-5-5 samples are 255, 280 and 310 mV, respectively. In addition, the Tafel slope of Mo_2N-Co_xN-5-0.5, Mo_2N-Co_xN-5-2 and Mo_2N-Co_xN-5-5 are about 121, 142 and 182 mV dec^{-1}, respectively. The above results indicate that the 2D porous Mo_2N-Co_xN-5 heterojuncion shows the lowest overpotential and smallest Tafel slope among various control samples, further suggesting the importance of constructing suitable interface for high-effective OER.

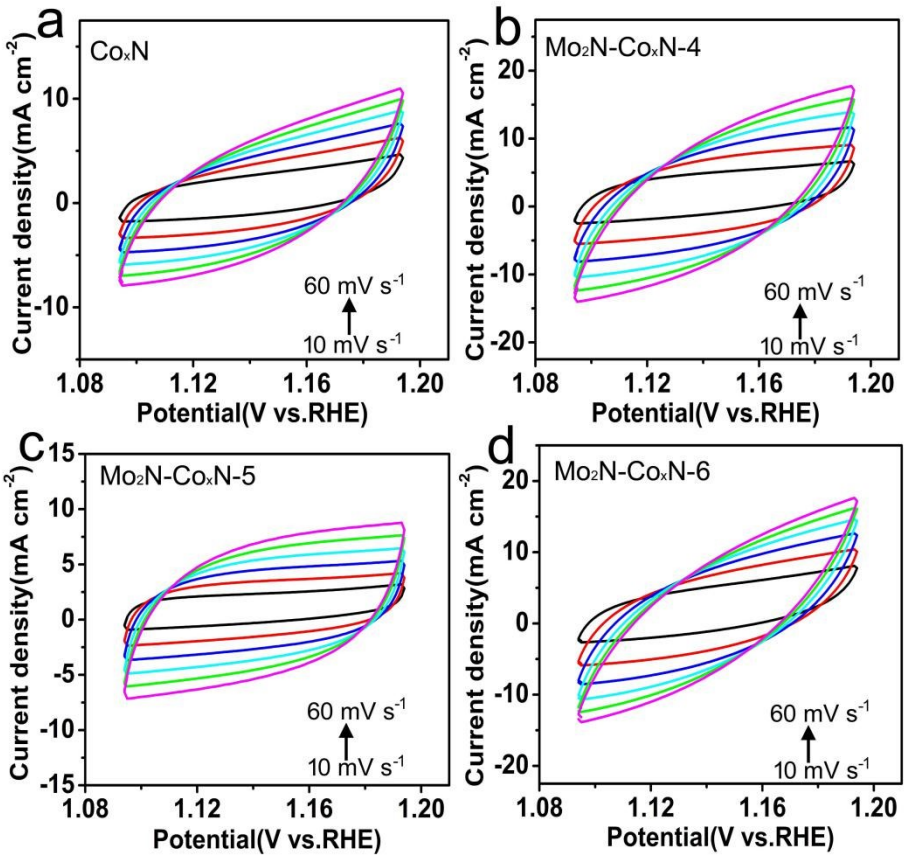

Figure S30. CVs of the catalysts recorded from 1.09 to 1.19 V at different rates from for 10 to 60 mV s^{-1} for (a) Co_xN and (b) Mo_2N-Co_xN-4, (c) Mo_2N-Co_xN-5, and (b) Mo_2N-Co_xN-6 in 1.0 M KOH for OER.

The C_{dl} value can be extracted from CV curves against different scan rates. In particular, the current responses in the voltage window of 1.09 to 1.19 V vs. RHE are recorded with an increased scan rate from 10 mV s^{-1} to 60 mV s^{-1}. The C_{dl} value for Mo_2N-Co_xN-5 is about 76.76 mF cm^{-2}. which is larger than those of Co_xN (51.57mF cm^{-2}), Mo_2N-Co_xN-4 (71.75 mF cm^{-2}), and Mo_2N-Co_xN-6 (46.94 mF cm^{-2}). 71.75 mF cm^{-2}, 46.94 mF cm^{-2}, 51.57 mF cm^{-2} of Mo_2N-Co_xN-4, Mo_2N-Co_xN-6, Co_xN. The high C_{dl} indicates the existence of more active sites in the Mo_2N-Co_xN-5 catalyst for OER.

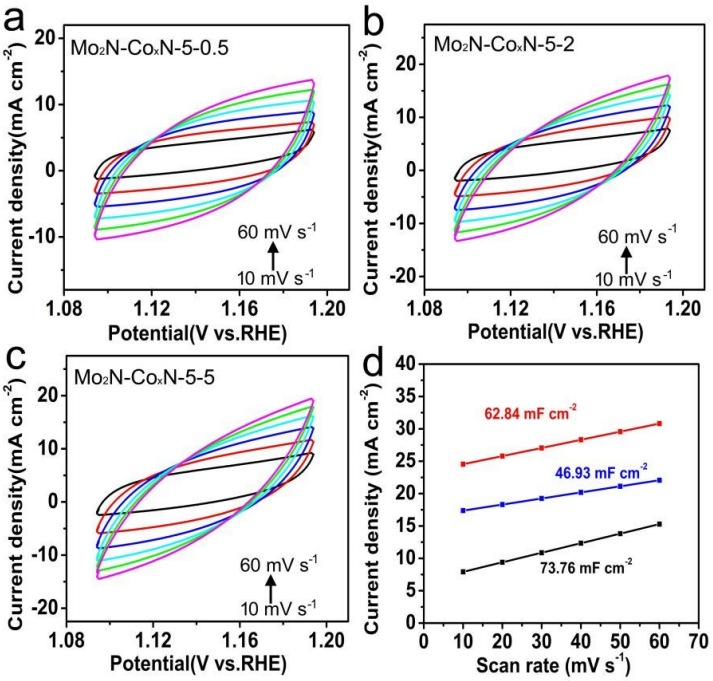

Figure S31. CVs of the catalysts recorded from 1.09 to 1.19 V at different rates from 10 to 60 mV s^{-1} for (a) Mo_2N-Co_xN-5-0.5, and (b) Mo_2N-Co_xN-5-2 and (c) Mo_2N-Co_xN-5-5 in 1.0 M KOH, and (d) The capacitive current at 1.14 V as a function of the scan rate for Mo_2N-Co_xN-5-0.5, Mo_2N-Co_xN-5-2 and Mo_2N-Co_xN-5-5 for OER.

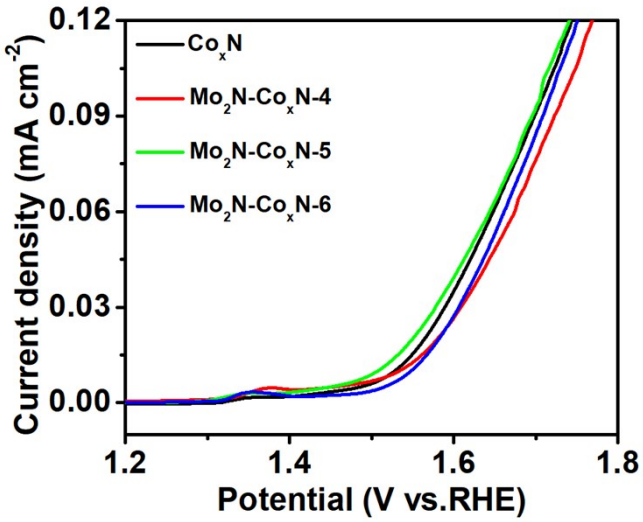

Figure S32. The LSV of Co_xN, Mo_2N-Co_xN-4, Mo_2N-Co_xN-5 and Mo_2N-Co_xN-6 for OER normalized by ECSA.

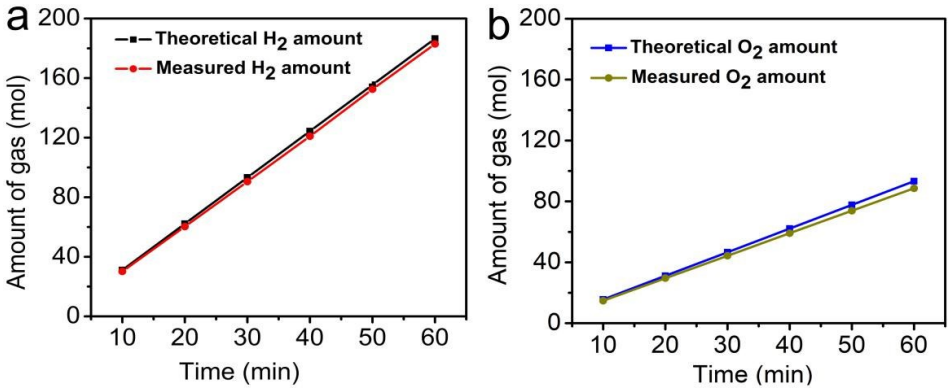

Figure S33. The experimentally determined and theoretically calculated amounts of H_2 and O_2 on Mo_2N-Co_xN-5. The Faradic efficiency (FE) is close to 100% for HER(a) and 95% for OER(b) at test of 60 min.

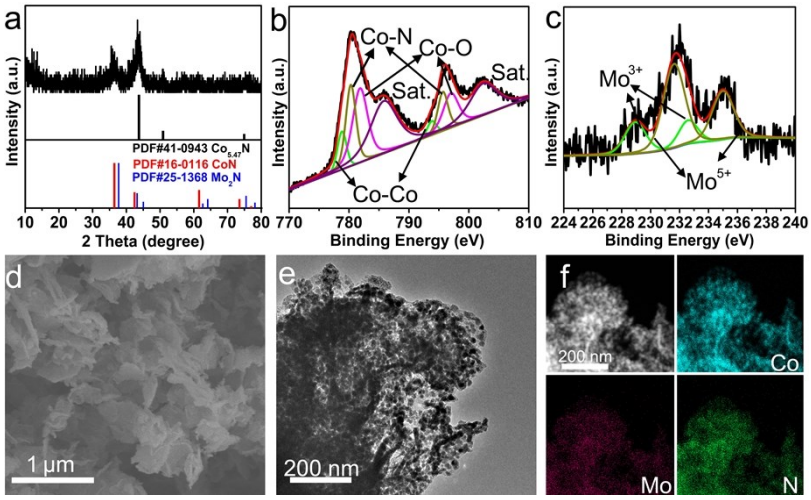

Figure S34. The XRD pattern (a), XPS spectra (b, c), SEM image (d), TEM image and corresponding EDS mapping (e, f) of Mo_2N-Co_xN-5 catalyst after the HER test.

The sample after HER was characterized to give further insight on the good HER performance. As shown in Figure S34, the XRD pattern shows similar peaks before and after the long-term HER test, indicating that the crystalline phase of the Mo_2N-Co_xN catalyst after HER process is nearly identical to the initial one. In addition, as displayed in Figure S34b and Figure S34c, the XPS spectra of Co 2p and Mo 3d are similar with the original one, implying the similar valence and coordination environments of Co and Mo in the catalyst before and after HER test. Also, as shown in Figure S34d and Figure S34e, there are no obvious change in morphology of Mo_2N-Co_xN catalyst after HER test. All of test show the good structural and composition stability of the Mo_2N-Co_xN catalyst towards the HER.

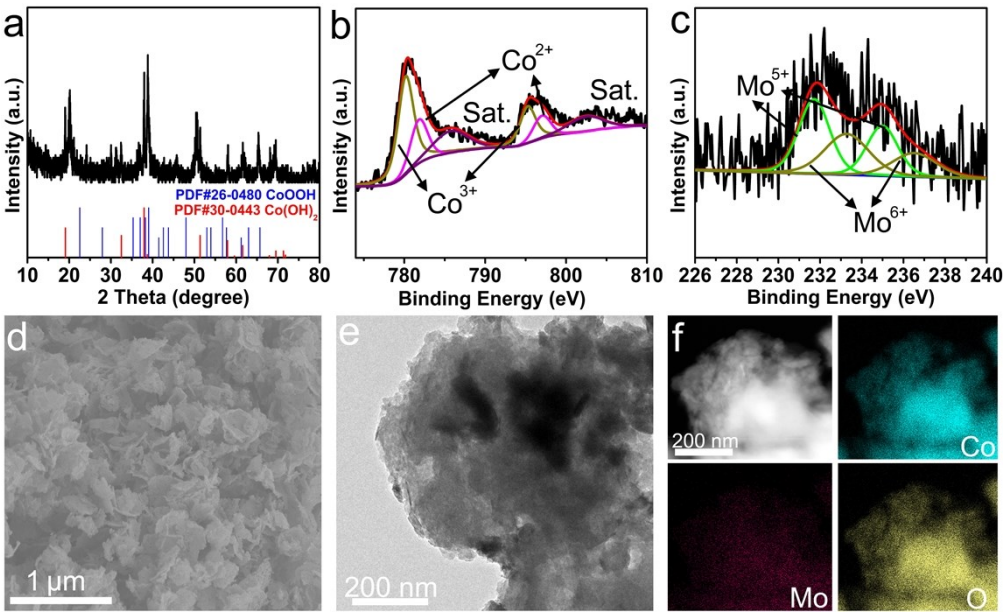

Figure S35. The XRD pattern (a), XPS spectra (b, c), SEM image (d), TEM image and corresponding EDS mapping (e, f) of Mo_2N-Co_xN-5 catalyst after the OER test.

We have performed the XRD, XPS and TEM test for the samples after the OER test. The catalyst show some obviously changes after OER process. As shown in Figure S35a, the XRD pattern of the sample after OER shows the obvious change compared with the original one. The diffraction peaks attributed to $Co(OH)_2$ and CoOOH can be seen. More details about chemical state changes can be obtained from the XPS spectra. As displayed in the Co 2p spectrum (Figure S35b), the content of Co^{3+} increased significantly, implying the cobalt in the sample is oxidized to high-valence Co oxide during the oxidation process. Also, the Mo species are also oxidized to high-valence Mo oxide after OER test (Figure S35c). Furthermore, SEM image (Figure S35d) shows the nanosheet structure for the samples after OER tests. However, the surface of the nanosheets (Figure S35e) shows some difference with that of original nanosheets, indicating the surface self-reconstruction of catalysts during OER. The tests shows the formation of oxides those were considered as active species for OER, which is consistent with the many previous studies.

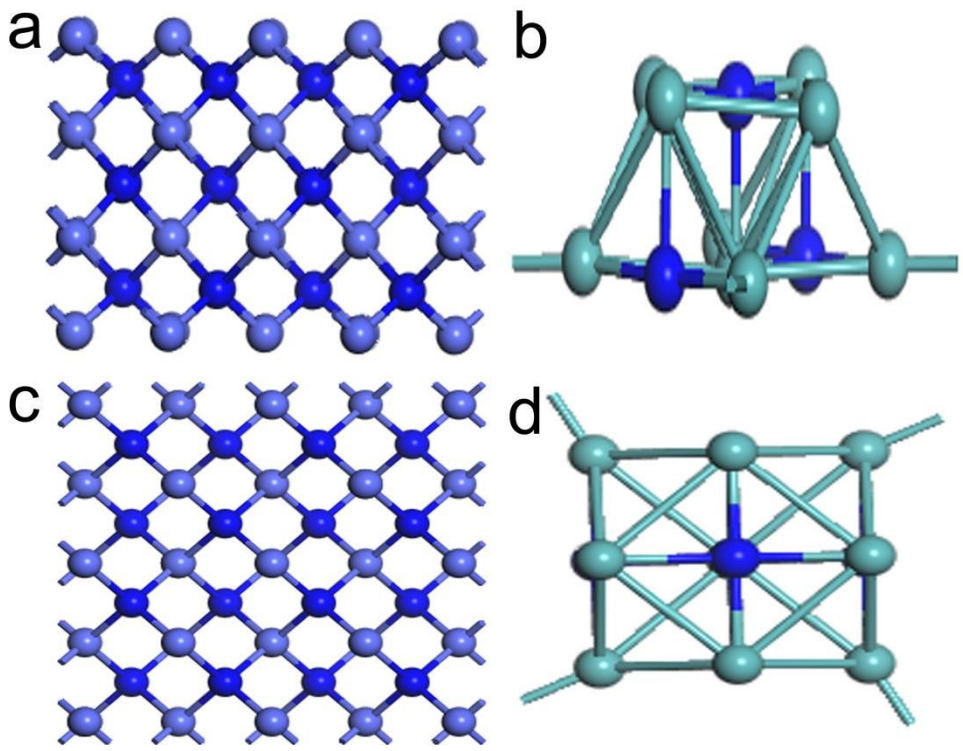

Figure S36. Side-view and Top-view schematic models of (a, c) CoN and (b, d) Mo_2N cluster.

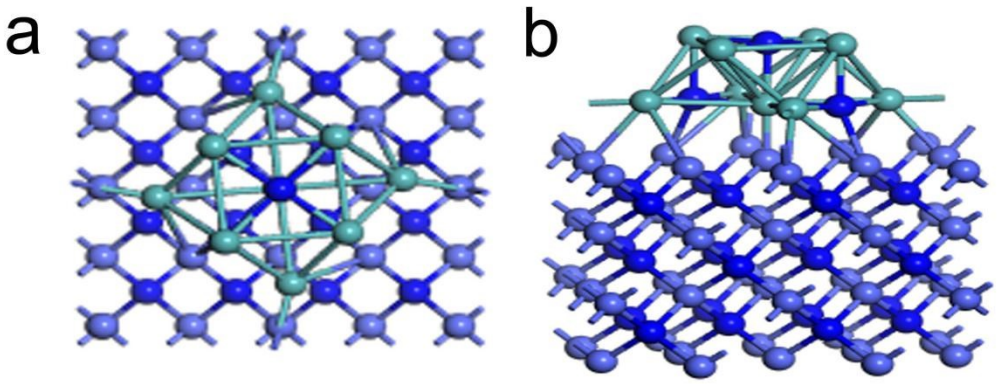

Figure S37. (a, b) Top-view and Side-view schematic models of Mo_2N-CoN.

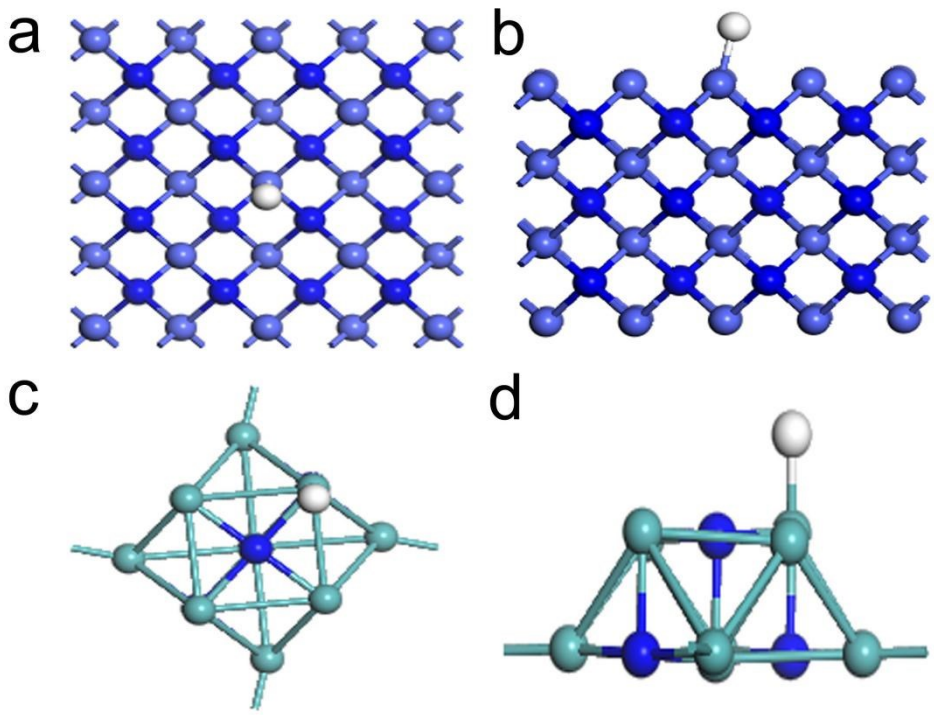

Figure S38. (a, c) Top-view schematic models of Mo_2N cluster and CoN with H* adsorbed on its surface, respective. (b, d) Side-view schematic models of Mo_2N cluster and CoN with H* adsorbed on its surface, respectively.

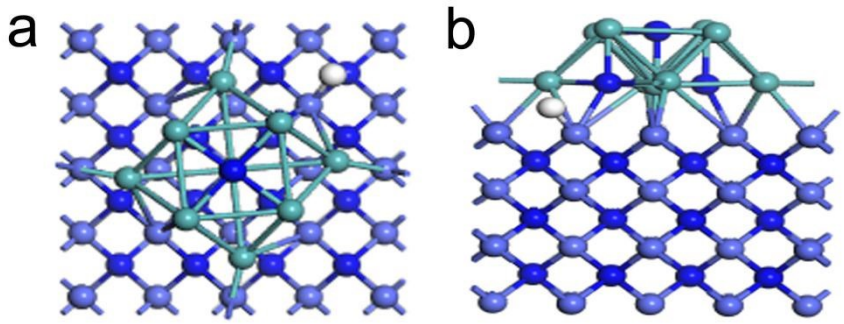

Figure S39. (a, b) Top-view and Side-view schematic models of Mo_2N-CoN (Co-2-site) with H* adsorbed on its surface.

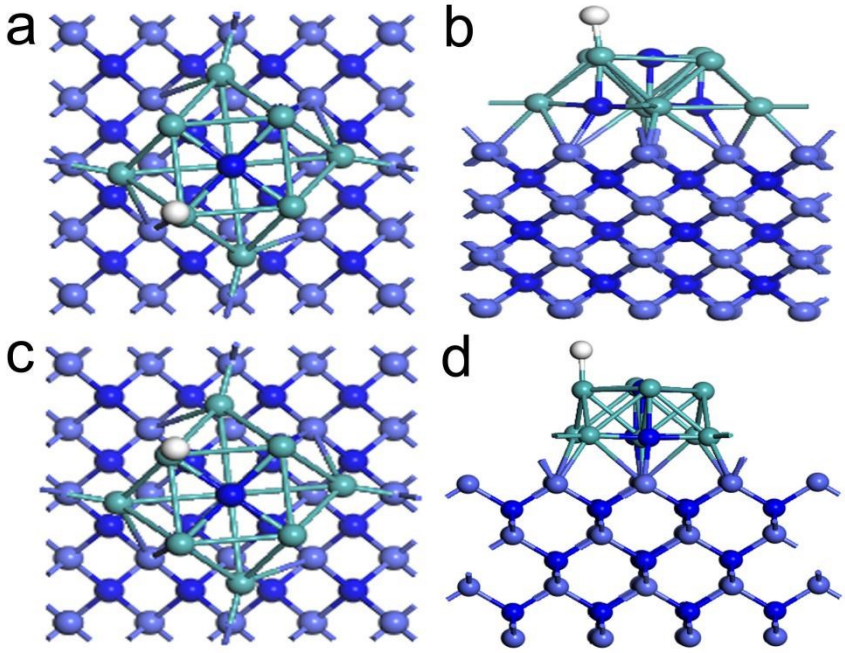

Figure S40. (a, b) Top-view and Side-view schematic models of Mo_2N-CoN (Mo-1-site) with H* adsorbed on its surface. (c, d) Top-view and Side-view schematic models of Mo_2N-CoN (Mo-2-site) with H* adsorbed on its surface.

Table S2. The HER performance of different catalysts in 1M KOH medium (IR represents the "90% IR compensation").

Catalyst	η_{10} (mV)	η_{100} (mV)
Mo_2N-Co_xN-4	120	350
Mo_2N-Co_xN-4 (IR)	98	215
Mo_2N-Co_xN-5	29	210
Mo_2N-Co_xN-5 (IR)	26	159
Mo_2N-Co_xN-6	57	260
Mo_2N-Co_xN-6(IR)	34	177
Co_xN	163	367
Co_xN (IR)	107	234
Pt/C	18	137

Table S3. Comparison of HER performance of Mo_2N-Co_xN-5 with other non-noble metal HER electrocatalysts in alkaline condition.

Catalyst	Current density (j) (mA cm^{-2})	Overpotential at corresponding J (mV)	Reference
Mo_2C Nanotube	10	112	*Angew. Chem. Int. Ed.,* **2015**, *54*, 15395
Mo_xC	10	128	*Nanoscale,* **2017**,*9*,7260–7267
Co_2P/CoN-in-NCNTs	10	98	*Adv. Funct. Mater.,* **2018**, *28*, 1805641
NiP_2/$NiSe_2$	10	93	*Appl. Catal. B Environ.,* **2021**, 282, 119584
$Co_{5.47}N$ NP@N-PC	10	149	*ACS Appl. Mater. Interfaces,* **2018**, *10*, 7134−7144

Co-MoS_2-1.4	10	56	*Adv. Energy Mater.,* **2020**, 2000291
$NiCo_2N$	10	48	*J. Mater. Chem. A,* **2019**, *7*, 19728–19732
CoMoC	10	46	*J. Mater. Chem. A,* **2019**, *7*, 12434–12439
Ni_3N-NiMoN	10	31	*Nano Energy,* 44 (**2018**) 353-363
Ni-P/Ni/NF	10	129	*Appl. Catal. B Environ.,* **2021**, 282, 119609
Co–Mo_2N	10	76	*J. Mater. Chem. A,* **2018**, *6*, 20100-20109
CoP/Co-MOF	10	34	*Angew. Chem. Int. Ed.,* **2019**, *58*, 4679-4684
Co/WN-600	10	27	*J. Mater. Chem. A,* **2020**, 7488-7496
Mo_2N-Mo_2C/Gr	10	154	*Adv. Mater.,* **2018**, *30*, 1704156
Mo_2N-Co_xN-5	10	29	***This work***

Table S4. The OER performance of different catalysts (IR represents the "90% IR compensation").

Catalyst	**η_{10} (mV)**	**η_{100} (mV)**
Mo_2N-Co_xN-4	271	458
Mo_2N-Co_xN-4(IR)	238	330
Mo_2N-Co_xN-5	247	424
Mo_2N-Co_xN-5(IR)	231	323
Mo_2N-Co_xN-6	310	471
Mo_2N-Co_xN-6(IR)	262	341
Co_xN	285	449
Co_xN(IR)	253	339
RuO_2	319	506

Table S5. Comparison of OER performance of Mo_2N-Co_xN-5 with other non-noble metal OER electrocatalysts in alkaline conditions.

Catalyst	Current density (j) (mA cm^{-2})	Overpotential at corresponding j (mV)	Reference
Ni-Mo nitride	10	295	*J. Mater. Chem. A*, **2017**, 13648
$NiCo_2O_4$	10	290	*Angew. Chem. Int. Ed.*, **2016**, 55, 6290
MoS_2/Ni_3S/Ni foam	10	218	*Angew. Chem. Int. Ed.*, **2016**, 128, 6814
Co_9S_8	10	320	*Adv. Funct. Mater.*, **2017**, 1606585
Co_3O_4/N-graphene	10	310	*Nature Materials*, 10, **2011**, 780-786
Co_4N nanowire arrays	10	260	*Angew. Chem. Int. Ed.,* **2015**, 127, 14923
Co-Mo_2C-CN_x-2	10	338	*Appl. Catal. B Environ.,* **2020**, 119738
Co@Co_3O_4/NC	10	410	Angew. Chem. Int. Ed., **2016**, 55,4087 -4091
Porous MoO_2 needs	10	260	*Advanced Materials,* **2016**, 28(19): 3785-3790
PMo/ZIF-67-6	10	295	*Chem. Sci.*, **2018**, 9, 4746-4755
Co–Mo_2N	10	296	*J. Mater. Chem. A,* **2018**, 6, 20100-20109
Ni_3N-NiMoN	10	277	*Nano Energy* 44 (**2018**) 353-363
$MoNi_4$/Ni foam	10	280	*J.Mater.Chem.A,* **2017**, 5, 2508
Mo_2N-Co_xN-5	10	247	***This work***

Table S6. Comparison of the overall water splitting performance of this work in alkaline electrolytes with literature reports.

Catalyst	Overall water splitting cell voltage (10 mA cm^{-2})	Reference
$CoNi(OH)_x$/Cu Foil	1.65	*Adv. Energy Mater.*, 2016, 6, 1501661.
MoO_2/NF	1.52	*Adv. Mater.,* 2016, 28, 3785.
Co-Mo_2C-CN_x-2	1.68	*Appl. Catal. B Environ.,* **2020**, 119738
PMo/ZIF-67-6-6N	1.61	*Chem. Sci.*, 2018, 9, 4746–4755
$Co_{5.47}N$ NP@N-PC	1.62	*ACS Appl. Mater. Interfaces* 2018, 10, 7134−7144
Ni/$Ni(OH)_2$	1.59	*Adv. Mater.,* 2020, 32, 1906915
CoP/NCNHP	1.64	*J. Am. Chem. Soc.,* 2018, 140, 2641-2618
FeCo/Co_2P	1.68	*Adv. Energy Mater.,* 2020, 1903854
Ni_3N-NiMoN	1.54	*Nano Energy* 44 (2018) 353–363
Mo_2N-Co_xN-5	1.53	***This work***